日本磁気学会
ISSN 2432-0250
Journal of the Magnetics Society of Japan
Electronic Journal URL: https://www.jstage.jst.go.jp/browse/msjmag

Vol.43 No.3 2019

Journal

JOURNAL OF THE MAGNETICS SOCIETY OF JAPAN

Vol.43 No.3 2019

日本磁気学会

ISSN 2432-0250

HP: http://www.magnetics.jp/ e-mail: msj@bj.wakwak.com
Electronic Journal: http://www.jstage.jst.go.jp/browse/msjmag

世界初！
高温超電導型VSM

新製品

世界初*、高温超電導マグネットをVSMに採用することで
測定速度 当社従来機1/20を実現。
0.5mm cube磁石のBr, HcJ高精度測定が可能と
なりました。
*2014年7月 東英工業調べ

測定結果例

高温超電導VSMによるNdFeB(sint.) 0.5mm cube BHカーブ

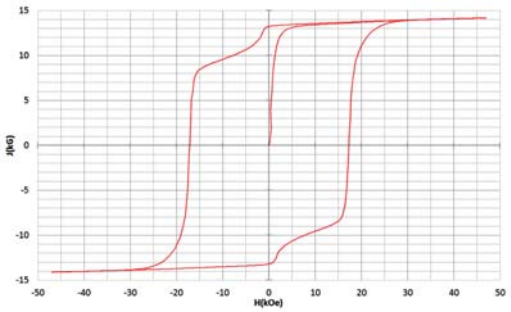

磁化測定レンジ：0.2emu
Br = 13.2kG　　HcJ = 17.2kOe

高温超電導VSMによるNdFeB(sint.) 1mm cube BHカーブ

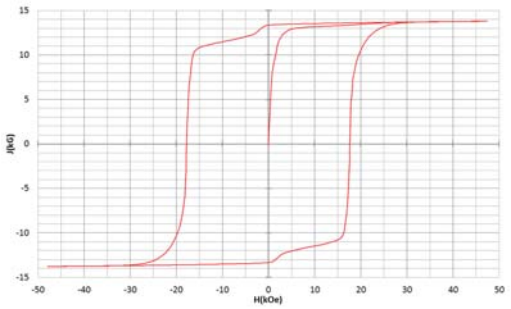

磁化測定レンジ：2emu
Br = 13.3kG　　HcJ = 17.7kOe

高温超電導VSMによるNdFeB(sint.) 4mm cube BHカーブ

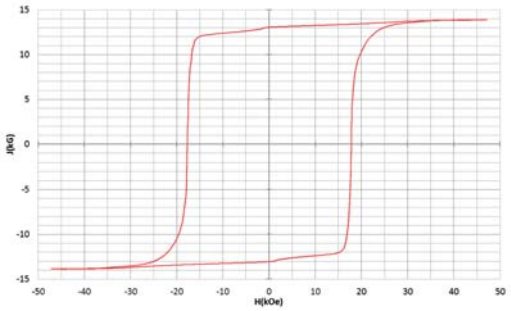

磁化測定レンジ：100emu
Br = 13.1kG　　HcJ = 17.8kOe

高速測定を実現

高温超電導マグネット採用により、高速測定を実現しました。Hmax= 5Tesla, Full Loop 測定が2分で可能です。
（当社従来機：Full Loop測定　40分）

小試料のBr,HcJ高精度測定

0.5mm cube 磁石のBr,HcJ高精度測定ができ、表面改質領域を切り出しBr,HcJの強度分布等、微小変化量の比較測定が可能です。
また、試料の加工劣化の比較測定が可能です。

試料温度可変測定

−50℃～+200℃温度可変UNIT（オプション）

磁界発生部の小型化

マグネットシステム部寸法：0.8m×0.3m×0.3m

TOEI 東英工業株式会社
http://www.toeikogyo.co.jp
〒194-0035 東京都町田市忠生1-8-13
TEL：042-791-1211 FAX：042-792-0490
E-mail : sales@toeikogyo.co.jp

有限要素法解析ソフトウェア COMSOL Multiphysics®

COMSOL MULTIPHYSICS®

マルチフィジックスの進化論

無制限・強連成で実現象に即したシミュレーション事例のご紹介

永久磁石を利用した磁気軸受の解析例

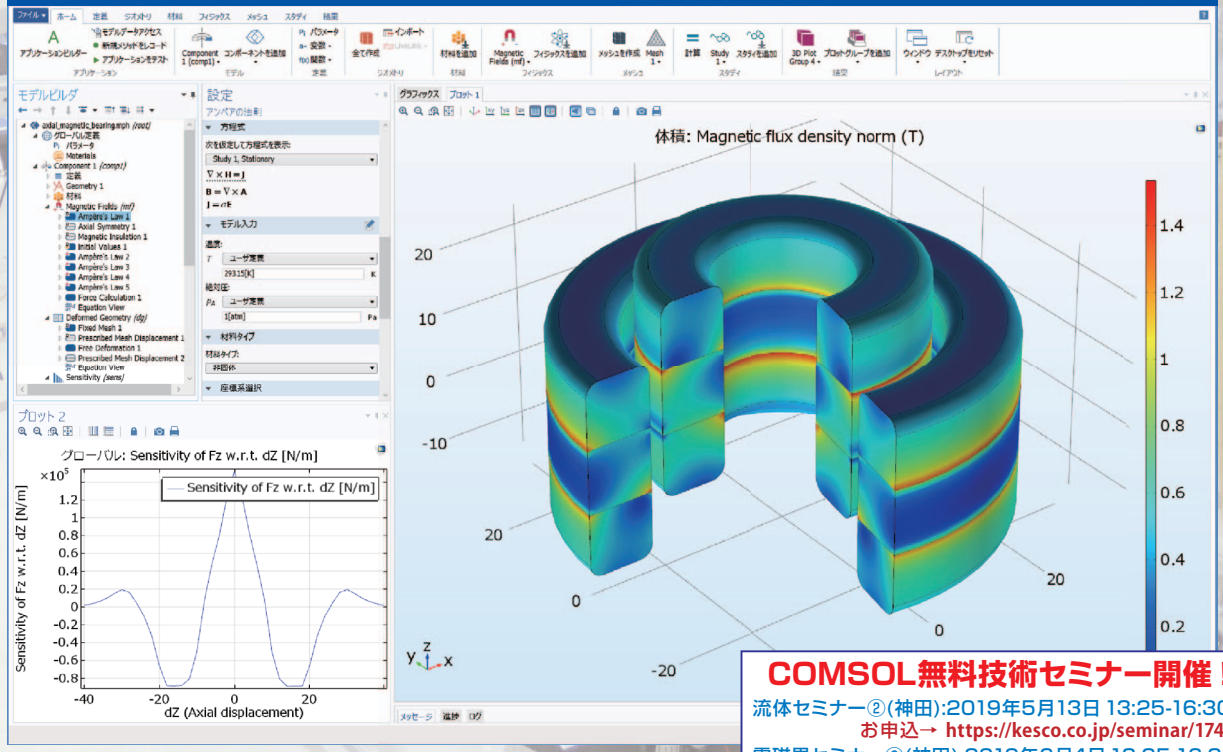

COMSOL無料技術セミナー開催！

流体セミナー②(神田):2019年5月13日 13:25-16:30
お申込→ https://kesco.co.jp/seminar/1745/
電磁界セミナー②(神田):2019年6月4日 13:25-16:30
お申込→ https://kesco.co.jp/seminar/1498/
各種セミナーのご案内→ https://kesco.co.jp/seminar/

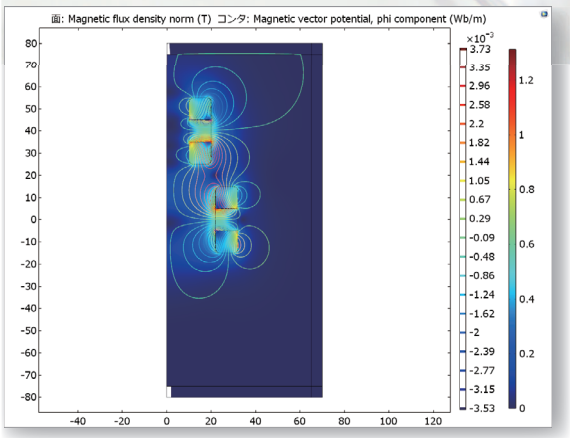

AC/DC モジュールの適用例

- AC/DC 電流分布、電場分布
- バイオヒーティング
- コイルとソレノイド
- SPICE 回路とフィールドシミュレーション
- 接触抵抗
- 電磁両立性 (EMC) および電磁妨害 (EMI)
- 電磁力およびトルク
- 電磁力シールド
- 電気機械の変形
- ホール効果を利用したセンサ
- インシュレータ、コンデンサ、誘電体
- モータ、ジェネレータ、および他の電気機械
- 非線形材料
- 寄生容量とインダクタンス
- 永久磁石と電磁石
- 多孔質材料
- 抵抗および誘導加熱
- センサ
- 超伝導体
- 変圧器とインダクタ

永久磁石を使用した磁気軸受の解析例

永久磁石を使用した軸受はターボ機械、ポンプ、モータ、発電機やフライホイール式エネルギー貯蔵システムなど、様々な分野で使用されています。非接触かつ潤滑不要で保守整備を大幅に省略できる点は、従来の機械式ベアリングと比べて重要なメリットです。
この例では、軸方向の永久磁石軸受の磁気力と剛性などの設計パラメータを計算する方法を示しています。

※AC/DCモジュールはCOMSOL Multiphysics®と併用するアドオン製品です。

COMSOL Multiphysics® なら、今まで不可能だった 3 種以上のマルチフィジックス解析を強連成で実現できます。30 日間全機能無料トライアル、無料の導入セミナー、1000種を超える世界の様々な事例をご提供いたします。詳しくは、下記の弊社営業部までお問い合せください。

COMSOL
http://www.comsol.jp

人とくるまのテクノロジー展 2019 横浜に出展します！
2019年5月22日-24日 10:00-18:00(最終日17:00まで)
会場：パシフィコ横浜 (神奈川県横浜市) ブース No.215
展示会の詳細はこちら→ https://expo.jsae.or.jp/

KESCO KEISOKU ENGINEERING SYSTEM
計測エンジニアリングシステム株式会社
https://kesco.co.jp/service/comsol/
Tel : 03-5282-7040 ・ Fax : 03-5282-0808

Journal of the Magnetics Society of Japan
Vol. 43, No. 3

Electronic Journal URL: https://www.jstage.jst.go.jp/browse/msjmag

CONTENTS

J. Magn. Soc. Jpn., **43**, 42-45 (2019)

Letter

Core losses of a nanocrystalline motor under inverter and sinusoidal excitations

A. Yao, T. Sugimoto*, and K. Fujisaki*
Department of Electrical and Computer Engineering, Toyama Prefectural University, *5180, Kurokawa, Imizu 939-0398, Japan*
*Department of Advanced Science and Technology, Toyota Technological Institute, *2-12-1, Hisakata, Tenpaku-ku, Nagoya 468-8511, Japan*

In this paper, we focus on an evaluation of core losses in permanent magnet synchronous motors (PMSMs) made of nanocrystalline magnetic materials under inverter and sinusoidal excitations. To discuss the core loss properties of a nanocrystalline motor, comparison with PMSMs made of amorphous magnetic materials and non-oriented (NO) silicon steel sheets is also performed. Under sinusoidal excitation, the core losses of the nanocrystalline motor were about 0.7 and 0.5 times smaller than those of the amorphous and NO motors, respectively. In particular, we found that the nanocrystalline motor reduced the core loss on the basis of time harmonic components in comparison with not only the NO motor but also the amorphous motor. On the basis of our results, the nanocrystalline motor is expected to be suitable for use in high-speed and high-frequency regions.

Key words: core loss, iron loss, nanocrystalline magnetic materials, PMSM, non-oriented steel sheets, amorphous magnetic materials

1 Introduction

The losses in the driving electric motors mainly consist of mechanical, copper, and core losses (iron losses). Recently, in order to reduce core losses of the motors, the motors based on core with amorphous magnetic materials (AMM) [1–12] and nanocrystalline magnetic materials (NMM) [13–15] have been developed and examined. NMM and AMM exhibit lower iron loss [16] than non-oriented (NO) silicon steel sheets. In particular, NMM offers potential reduction of core loss, compared to AMM. In our study, we examine core loss properties of the motor with NMM under inverter and sinusoidal excitations.

In order to control the rotational torque and speed of the motor, pulse width modulation (PWM) inverters are usually used. In the recent times, several researchers have shown that the iron losses of the magnetic core under PWM inverter excitation increase due to time harmonic components [17–29]. Therefore, it is necessary to estimate the influence of time harmonic components in the motor with NMM to develop the low loss motor systems.

Previous studies have addressed that the motor with NMM core exhibits low core losses "under PWM inverter excitation" [13,15]. Thus, the next phase is to correctly understand the core loss properties of the motor with NMM core "under sinusoidal excitation". Since the motor core loss under sinusoidal excitation does not have time harmonic components, the evaluation of the sinusoidal-excited motor can obtain the smallest core losses of the motor core at the same experimental conditions (the same speed, torque, and vector control method) [12].

In addition, by comparing losses under inverter and sinusoidal excitations, we can experimentally estimate the core losses caused by time harmonic components [12]. Because of a deterioration of the iron losses caused by the manufacture process and so on [15], it is difficult to accurately obtain the core loss of the NMM motor based on iron losses of the materials by numerical simulations. Therefore, based on the experimental results, it is important to estimate the core losses caused by time harmonic components of the motor with NMM.

This study focuses on the experimental evaluation of core losses of permanent magnet synchronous motor (PMSM) with NMM cores excited by inverter and sinusoidal inputs. In order to discuss the core loss properties of the PMSM with NMM, we compare the PMSMs with NO and with AMM under PWM inverter and sinusoidal excitations. By comparing core losses under inverter and sinusoidal excitations, we experimentally estimate core losses caused by higher harmonic components (in particular, time harmonic components) of the PMSM with NMM.

2 Experimental method

In our study, we use three kinds of motor cores. Figure 1 shows stator and rotor cores made of NMM (FT-3M), NO electrical steel sheets (35H300), and AMM (SA-1) that consist of Fe-Si-B-Cu-Nb, Fe-Si, and Fe-Si-B, respectively. Table 1 shows the specifications of three different materials used for those cores. From here on, the PMSMs with the stator and rotor cores made of NMM, NO sheets, and AMM is called NMM-PMSM, NO-PMSM, and AMM-PMSM, respectively. Here, these three PMSMs made of different materials are the same design. In these PMSMs, the Sm-Fe-B bonded magnets (S5P-12ME, Aichi Steel Corporation) are used. The stacking factors of NMM-, NO-, and AMM-cores are about 80 %, 100 %, and 90 %, respectively. Table 2 shows the characteristics of the motor (stator and rotor) cores. Figure 2 shows the schematic of cross-sectional view of motor cores. See Refs. [2,12,14,15] for the details of design and fabrication process of rotor and stator cores.

Figure 3 shows the schematic of the PMSM and its control system under no-load condition. Here, we can perform good accuracy of core loss measurement in no-load condition in comparison with the case in load condition [15]. By using this experimental system, we perform two excitation method tests. The first

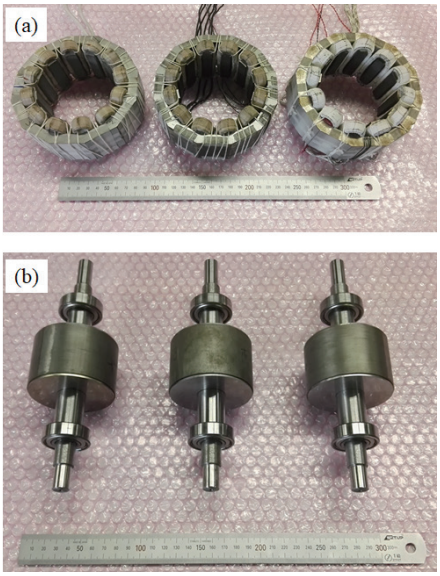

Fig. 1 Photographs of motor cores assembled with nanocrystalline magnetic materials (left, FT-3M), non-oriented (NO) silicon steel sheets (center, 35H300), and amorphous magnetic materials (right, SA-1). (a) stator and (b) rotor cores.

test is to measure the core loss of the PMSM excited by the three phase sinusoidal wave, which is supplied by three linear amplifiers (HSA 4014, NF). The second test is to measure the core loss of the PMSM excited by the PWM inverter wave using three phase PWM inverter (MWINV-9R122B, Myway). Here, a standard vector control is utilized for the speed control. See Refs. [12] for the details of the control method.

The core loss under no-load condition P_{core} is given by

$$P_{\mathrm{core}} = P_{\mathrm{in}} - P_{\mathrm{cu}} - P_{\mathrm{m}}, \tag{1}$$

$$P_{\mathrm{in}} = P_u + P_v + P_w, \tag{2}$$

$$P_{\mathrm{cu}} = (I_u^2 + I_v^2 + I_w^2)R, \tag{3}$$

where P_{in} denotes the active input power, P_{cu} is the copper loss, P_{m} is the mechanical loss, $I_{u,v,w}$ are respectively the u, v, and w rms currents, $P_{u,v,w}$ are respectively the u, v, and w input powers, and R (= 0.5 Ω) is the winding resistance. Here, the copper wire has a diameter of 1 mm. The approximation formula for the skin depth is given as $\sqrt{2\rho/\omega\mu}$, where ρ (= 1.68×10^{-8} Ω·m) is the resistivity, ω is the frequency, and μ (= 1.26×10^{-6} H/m) is the permeability. Here, the skin depth of the copper wire is obtained as about 1.5 mm at 2 kHz. Thus, it is thought that the copper wire is almost unaffected by the skin effect. In this study, by using a rotor without magnetization, the mechanical loss P_{m} is measured. In our study, the mechanical losses are estimated as about 0.34, 0.88, and 1.4 W at 750, 1500, and 2250 rpm, respectively (see Ref. [1] for the details of the mechanical loss measurement method.).

It is well known that the core loss under inverter excitation depends on fundamental, space harmonic, and time harmonic components. On the other hand, the core loss under sinusoidal excitation relates to only fundamental and space harmonic components. Thus, the core losses caused by time harmonic components W_{thc} can be obtained by [12]

$$W_{\mathrm{thc}} = W_{\mathrm{inv}} - W_{\mathrm{sin}}, \tag{4}$$

where W_{inv} denotes the core loss under PWM inverter excitation and W_{sin} is that under sinusoidal excitation.

Under PWM inverter excitation, the carrier frequency f_{c}, the switching dead-time, and the DC bus voltage V_{dc} are set to 1 kHz, 3500 ns, and 250 V, respectively. In our study, three rotational speeds (750, 1500, and 2250 rpm) are evaluated. The rotational speeds of 750, 1500, and 2250 rpm correspond to electrical frequencies of 50, 100, and 150 Hz, respectively. The PMSM under sinusoidal and inverter excitations shown in Fig. 3 is operated by zero d-axis current control. Note that the core losses caused by time harmonic components (space harmonic components) depend mainly on losses at about 2 kHz (at three times electrical frequency).

Table 1 Specifications of different materials used for cores.

	NMM	NO	AMM
Reference	FT-3M	35H300	SA-1
Density ϕ [kg/m^3]	7300	7650	7180
Composition	Fe-Si-B-Cu-Nb	Fe-Si	Fe-Si-B
Thickness [μm]	18	350	25
Relative permeability	70,000	1,400	5,000
Saturation magnetic flux density [T]	1.23	2.0	1.56

Table 2 Motor specifications.

Characteristic	Symbol	Value
Poles / Slot number		8 / 12
Radius of stator core	R_{s}	64 mm
Radius of rotor core	R_{r}	37 mm
Air gap	G	1.25 mm
Yoke width	W_{y}	9.2 mm
Tooth width	W_{t}	10 mm
Axial core length		47 mm
Permanent magnet length	L_{PM}	20 mm
Permanent magnet width	W_{PM}	2 mm
Winding method		Concentrated

3 Results and discussion

Figure 4 shows the core loss characteristics of three PMSMs with respect to the rotational speed under sinusoidal excitation. Here, the rms current values of the NMM- and AMM-PMSMs (NO-PMSM) are about 0.14, 0.16, and 0.18 A (0.13, 0.14, and 0.16 A) at 750, 1500, and 2250 rpm, respectively. Then the core losses are caused by fundamental and space harmonic compo-

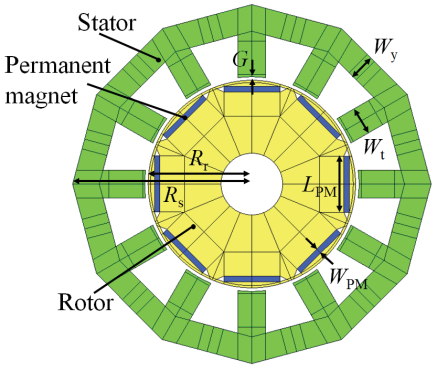

Fig. 2 Schematic of cross-sectional view of motor cores.

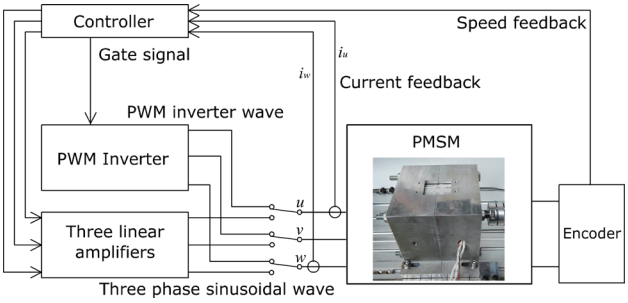

Fig. 3 Schematic of PMSM and its excitation (control) system. In our study, we use two excitation methods. One method is sinusoidal excitation by using three linear amplifiers and other method is inverter excitation by using three phase PWM inverter.

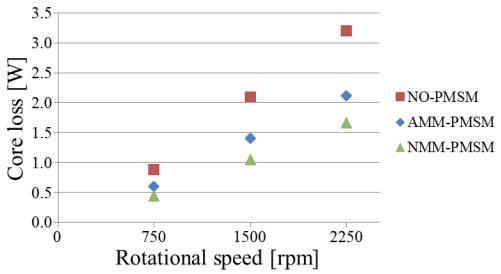

Fig. 4 Experimentally measured core losses of three PMSMs (NO, AMM, and NMM) as a function of rotational speed under sinusoidal excitation.

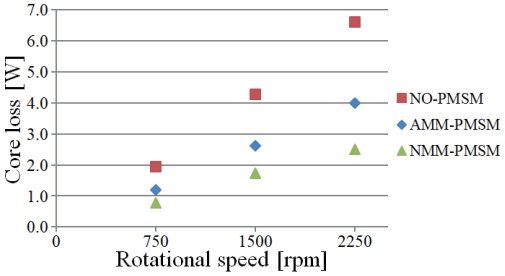

Fig. 5 Experimentally obtained core losses of three PMSMs with respect to rotational speed under inverter excitation.

nents. For each rotation speed, the NMM-PMSM exhibits excellent low core loss in comparison with that of the AMM- and NO-PMSMs. The NMM-PMSM excited by sinusoidal input exhibits

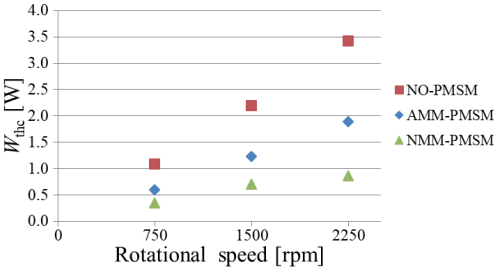

Fig. 6 Core losses caused by time harmonic components of three PMSMs with respect to rotational speed. These results were obtained from Eq. (4) on basis of experimental results.

core losses of about 0.43 W at 750 rpm, of about 1.0 W at 1500 rpm, and of about 1.7 W at 2250 rpm, respectively. Under sinusoidal excitation, the core loss of the NMM-PMSM is about 0.7 and 0.5 times smaller than that of the AMM- and NO-PMSMs, respectively.

Figure 5 shows the core loss properties of three PMSMs fed by inverter input as a function of the rotational speed. Here, the NO-PMSM (AMM-PMSM) exhibits the rms current of about 0.27, 0.51, and 0.80 A (0.31, 0.59, and 0.92 A) at 750, 1500, and 2250 rpm, respectively. The rms current values of the NMM-PMSM at 750, 1500, and 2250 rpm are about 0.33, 0.63, and 0.99 A, respectively. For sinusoidal and inverter excitations, the current caused by fundamental wave is almost the same value. See Appendix for the details of waveforms, magnetic flux density, and the related values. Under inverter excitation, the core losses are caused by fundamental, time harmonic and space harmonic components. In the experiments, the tested NMM-PMSM presents small core loss in comparison with that of the AMM- and NO-PMSMs. The core losses of the NMM-PMSM are 0.78 W at 750 rpm, 1.7 W at 1500 rpm, and 2.5 W at 2250 rpm, respectively. The core losses of the NMM-PMSM is about 0.6 and 0.4 times of those of the AMM- and NO-PMSMs, respectively. Here, the magnet losses of the PMSMs accounts for less than 1 % of the total core losses [15] because the Sm-Fe-B bonded magnets have extremely low loss.

We now discuss the core losses caused by time harmonic components of three PMSMs obtained with Eq. (4). Figure 6 shows the obtained W_{thc} results at each measurement point. The core losses caused by time harmonic components of the NMM-PMSM are drastically smaller than those of the AMM- and NO-PMSMs. The average core loss reduction caused by time harmonic components of the NMM- and AMM-PMSMs under PWM inverter excitation is about 70% and 45% as compared to the core loss of the NO-PMSM, respectively. In average, the W_{thc} of the NMM-, AMM-, and NO-PMSMs accounts for 40 %, 48 %, and 53 % of the core losses, respectively. Thus, we found that the NMM-PMSM can achieve core loss reduction caused by time harmonic components, which correspond to losses in the high-frequency region, in comparison with not only the NO-PMSM but also the

AMM-PMSM. Therefore, the NMM-PMSM is expected to be suitable for use in high-speed and high-frequency regions.

4 Conclusion

We for the first time examined the fabricated nanocrystalline motor under both sinusoidal and inverter excitations. In addition, the NO and amorphous motors were compared to discuss the core loss properties of the nanocrystalline motor. Under sinusoidal excitation, the core loss of the NMM-PMSM was about 0.7 and 0.5 times smaller than that of the AMM- and NO-PMSMs, respectively. In particular, we found that the NMM-PMSM can realize core loss reduction caused by time harmonic components, which correspond to high-frequency region, in comparison with not only the NO-PMSM but also the AMM-PMSM. These results open the way to further research for ultimate low loss motor system based on the nanocrystalline motor, especially in the high-speed motor. In our future works, we will perform the evaluation of building factor [21,30] to understand the core losses of the PMSM caused by factors such as the manufacturing process based on both experiments and numerical simulations. In near future, we will examine the core loss, the rated power, the rated torque, the torque capacity, and the efficiency properties under load condition. The more precise measurement of mechanical loss and the loss and current for each frequency will be investigated.

Acknowledgment This work was partly supported by the Ministry of Education, Culture, Sports, Science and Technology Program, Japan, for private universities, the Nagamori Foundation Research Grant, JFE 21st Century Foundation, JSPS KAKENHI Grant Number 18K13749, 18K04112, and the New Energy and Industrial Technology Development Organization (NEDO).

References

1) N. Denis, Y. Kato, M. Ieki, and K. Fujisaki: *AIP Adv.*, **6**, 055916 (2016).
2) S. Okamoto, N. Denis, Y. Kato, M. Ieki, and K. Fujisaki: *IEEE Trans. Ind. Appl.*, **52**, 2261 (2016).
3) M. Dems and K. Komeza: *IEEE Trans. Ind. Electron.*, **61**, 3046 (2014).
4) A. Chiba, H. Hayashi, K. Nakamura, S. Ito, K. Tungpimolrut, T. Fukao, M. A. Rahman, and M. Yoshida: *IEEE Trans. Ind. Appl.*, **44**, 699 (2008).
5) Z. Wang, Y. Enomoto, R. Masaki, K. Souma, H. Itabashi, and S. Tanigawa: Proc. ICPE 2011 - ECCE Asia, Jeju, 2011, p. 1940 (IEEE, 2011).
6) G. S. Liew, W. L. Soong, N. Ertugrul, and J. Gayler: Proc. AUPEC 2010, Christchurch, 2010, p. 1 (IEEE, 2010).
7) Z. Wang, Y. Enomoto, M. Ito, R. Masaki, S. Morinaga, H. Itabashi, and S. Tanigawa: *IEEE Trans. Magn.*, **46**, 570 (2010).
8) Z. Wang, R. Masaki, S. Morinaga, Y. Enomoto, H. Itabashi, M. Ito, and S. Tanigawa: *IEEE Trans. Ind. Appl.*, **47**, 1293 (2011).
9) Y. Enomoto, M. Ito, H. Koharagi, R. Masaki, S. Ohiwa, C. Ishihara, and M. Mita: *IEEE Trans. Magn.*, **41**, 4304 (2005).
10) T. Fan, Q. Li, and X. Wen: *IEEE Trans. Ind. Electron.*, **61**, 4510 (2014).
11) R. Kolano, K. Krykowski, A. Kolano-Burian, M. Polak, J. Szynowski, and P. Zackiewicz: *IEEE Trans. Magn.*, **49**, 1367 (2013).
12) A. Yao, T. Sugimoto, S. Odawara, and K. Fujisaki: *AIP Adv.*, **8**, 056804 (2018).
13) N. Nishiyama, K. Tanimoto, and A. Makino: *AIP Adv.*, **6**, 055925 (2016).
14) N. Denis, M. Inoue, K. Fujisaki, H. Itabashi, and T. Yano: *IEEE Trans. Magn.*, **53**, 1 (2017).
15) A. Yao, T. Sugimoto, S. Odawara, and K. Fujisaki: *IEEE Trans. Magn.*, **54**, 1 (2018).
16) A. Yao, K. Tsukada, and K. Fujisaki: *IEEJ J. Ind. Appl.*, **7**, 321 (2018).
17) M. Kawabe, T. Nomiyama, A. Shiozaki, H. Kaihara, N. Takahashi, and M. Nakano: *IEEE Trans. Magn.*, **48**, 3458 (2012).
18) K. Fujisaki and S. Liu: *J. Appl. Phys.*, **115**, 17A321 (2014).
19) S. Odawara, K. Fujisaki, and F. Ikeda: *IEEE Trans. Magn.*, **50**, 1 (2014).
20) T. Taitoda, Y. Takahashi, and K. Fujiwara: *IEEE Trans. Magn.*, **51**, 1 (2015).
21) A. Yao, K. Tsukada, S. Odawara, K. Fujisaki, Y. Shindo, N. Yoshikawa, and T. Yoshitake: *AIP Adv.*, **7**, 056618 (2017).
22) A. Boglietti, P. Ferraris, M. Lazzari, and M. Pastorelli: *IEEE Trans. Magn.*, **32**, 4884 (1996).
23) A. Boglietti, P. Ferraris, M. Lazzari, and F. Profumo: *IEEE Trans. Magn.*, **27**, 5334 (1991).
24) A. Boglietti, P. Ferraris, M. Lazzari, and M. Pastorelli: *IEEE Trans. Magn.*, **31**, 4250 (1995).
25) W. A. Roshen: *IEEE Trans. Power Electron.*, **21**, 1138 (2006).
26) W. A. Roshen: *IEEE Trans. Power Electron.*, **22**, 30 (2007).
27) A. Yao, K. Tsukada, and K. Fujisaki: Proc. LDIA 2017, Osaka, 2017, p. 1 (IEEE, 2017).
28) A. Yao and K. Fujisaki: Proc. LDIA 2017, Osaka, 2017, p. 1 (IEEE, 2017).
29) A. Yao, S. Odawara, and K. Fujisaki: *IEEJ J. Ind. Appl.*, **7**, 298 (2018).
30) A. Yao, A. Adachi, and K. Fujisaki: Proc. IEMDC 2017, Miami, 2017, p. 1 (IEEE, 2017).

Appendix: Waveforms and magnetic flux density

Appendix Figs. 1 (a) and (b) show voltage and current waveforms at 750 rpm of three PMSMs under PWM inverter excitation. Here, the maximum magnetic flux densities in the teeth parts of the NMM-, NO-, and AMM-PMSMs (under both excitations) are about 0.6, 0.4, and 0.5 T, respectively. The average difference between magnetic flux densities under sinusoidal and inverter excitations is about 3 % or less.

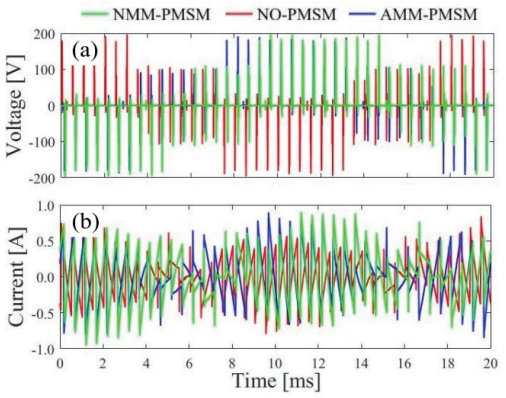

Appendix Fig. 1 Waveforms under inverter excitation at 750 rpm: (a) voltage, (b) current.

Recieved Jan. 21, 2019; Accepted Feb. 15, 2019

J. Magn. Soc. Jpn., **43**, 46-49 (2019)

Letter

Iron Loss and Hysteresis Properties under High-Temperature Inverter Excitation

A. Yao and T. Hatakeyama
Department of Electrical and Computer Engineering, Toyama Prefectural University, *5180, Kurokawa, Imizu 939-0398, Japan*

We experimentally and numerically examined the magnetic properties of magnetic materials under room- and high-temperature inverter excitations. We show that the iron loss and hysteresis properties of magnetic materials under pulse width modulation (PWM) inverter excitation depend strongly on the temperature dependence of semiconductor characteristics. The iron loss under PWM inverter excitation decreased as the temperatures of semiconductors (Si-insulated gate bipolar transistors and Si-diodes) increased. In addition, it was found that the rate of change of iron loss based on the temperature dependence of semiconductor characteristics at a high carrier frequency was larger than that at a low carrier frequency.

Key words: iron loss, hysteresis property, inverter, high-temperatures, play model

1 Introduction

High-temperature (HT) motor drive systems have been used in harsh temperature environments such as automotive, aerospace, and fire sites [1–3]. In the motor drive system, in order to control the rotational speed, pulse width modulation (PWM) inverters are normally utilized. Several researchers have recently shown that due to the higher harmonic components the iron losses in the magnetic core under PWM inverter excitation increase in comparison with sinusoidal case [4–14]. In the HT motor system, the inverter and magnetic material cores are exposed to HT. To realize HT and high efficiency motor drive system, it is to understand magnetic properties of magnetic materials fed by inverter in harsh temperature environments. To separate the effects of temperature properties of the semiconductors and the magnetic materials on the magnetic properties, it is necessary to consider the following two steps: (1) to evaluate magnetic properties of "magnetic materials at HT" under "room temperature (RT) inverter" excitation and (2) to investigate magnetic properties of "magnetic materials at RT" fed by "HT inverter". In the recent times, we have examined magnetic properties in magnetic materials at HT under "RT inverter" excitation[12,15]. The next step is to understand magnetic properties of RT magnetic materials fed by "HT inverter". This paper aims to estimate the iron loss and hysteretic properties of a non-oriented (NO) material, which is conventionally used as the motor core, under RT and "HT inverter" excitations.

We recently have shown that the power semiconductor properties affect iron loss and hysteresis properties of magnetic materials under PWM inverter excitation[16,17]. It is well known that the power semiconductor properties depend strongly on the temperature. Here, in order to estimate the relation between power semiconductor and iron losses properties under HT inverter excitation, it is necessary to correctly understand the influence of carrier frequency that relates to the number of switching times.

In this paper, we experimentally and numerically examine the iron losses and hysteretic properties of magnetic materials under RT and HT (300°C) inverter excitations. This paper addresses the experimental iron loss properties as a function of carrier frequency of a NO ring excited by HT inverter. Furthermore, by using the play model[18–20] with the Cauer circuit[15,21–25] which takes into account power semiconductor properties[26], we numerically investigate the magnetic hysteretic properties under RT and HT inverter excitations.

2 Experimental and numerical methods

Figure 1 shows a schematic of the experimental setup used to measure the iron loss characteristics under RT and HT inverter excitations. The single phase PWM inverter consists of Si-insulated gate bipolar transistors (IGBT) and Si-diodes (GT20J341). We use a ring specimen made of laminations of standard NO electrical steel sheets (35H300) [11]. Here, the semiconductors (Si-IGBTs and Si-diodes) of the inverter are exposed to ambient temperature variations in a temperature-controlled oven (STH-120) to evaluate iron loss properties based on the temperature dependence of the semiconductor characteristics. Note here that the ring specimen (magnetic core) is set at RT. This ring specimen has two (primary and secondary) coils wound with round wires that are used as an exciting-coil and a *B*-coil. Tab. 1 shows the characteristics of the ring specimen and semiconductors.

In the experiments, by integrating H and B, the iron losses W_{ring} of the ring specimen are given by[15,17]

$$W_{\mathrm{ring}} = \frac{1}{T\rho}\int H\mathrm{d}B, \tag{1}$$

$$H = \frac{N_1 I}{l}, \tag{2}$$

$$B = \frac{1}{N_2 S}\int V dt, \tag{3}$$

where ρ (= 7650 kg/m^3) denotes the density of the NO electrical steel sheet, T (= 0.02 s) is the period, N_1 (= 264) is the number of turns of the exciting coil, l (= 0.36 m) is the magnetic path length, N_2 (= 264) is the number of turns of *B*-coil, S (= 87.5 mm^2) is the cross section area of the ring, I is the current flowing in the primary coil of the ring specimen, and V is the *B*-coil voltage.

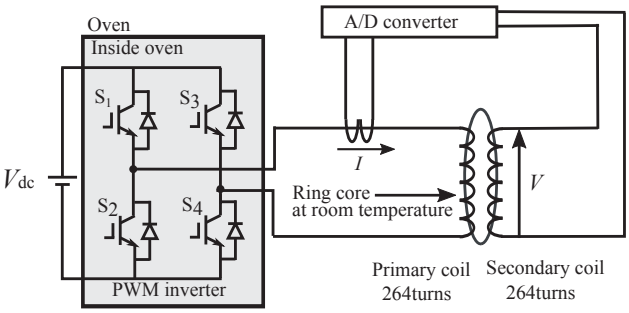

Fig. 1 Schematic of ring specimen, inverter, and measurement system for obtaining the experimental iron loss and hysteresis properties under room-temperature (RT) and high-temperature (HT) inverter excitations. Semiconductors (Si-IGBTs and Si-diodes) of inverter were set in oven and exposed to ambient temperature variations. Ring core was set at RT.

Table 1 Specifications of ring specimen and semiconductors.

Characteristic	Symbol	Value
Material		35H300
Density	ρ	7650 kg/m^3
Cross section area	S	87.5 mm^2
Height	d	7 mm
Average magnetic path length	l	0.36 m
Primary coil winding	N_1	264 turns
Secondary coil winding	N_2	264 turns
Semiconductors		GT20J341

By using Eq. (1), we can calculate the iron loss caused by both fundamental and higher harmonic components. In the following experiments and numerical simulations of ring tests, the modulation index, the maximum magnetic flux density of the ring, and the switching dead time are set to 0.5, 0.2 T, and 3500 ns, respectively. The fundamental frequency f_0 is set to 50 Hz. The ring tests are carried out at carrier frequencies f_c of 1, 4, 12, and 20 kHz. See refs. [15,17] for the details of the iron loss measurements.

In our paper, the rate of change of iron loss η based on semiconductor temperature is defined by

$$\eta = \frac{W_{\mathrm{ring}}^{\mathrm{RT}} - W_{\mathrm{ring}}^{300}}{W_{\mathrm{ring}}^{\mathrm{RT}}}, \tag{4}$$

where $W_{\mathrm{ring}}^{\mathrm{RT}}$ and W_{ring}^{300} are the iron losses at RT and 300°C, respectively.

In our paper, in order to measurement the temperature dependence of $I-V$ characteristics of the semiconductors (Si-IGBTs and Si-diodes), we use the series precision source/measure unit (SMU) (B2902A, Keysight). The Si-devices under test are placed inside the oven (STH-120) and are exposed to ambient temperature variations.

In order to express hysteretic properties under RT and HT inverter excitations by numerical simulations, we use the dynamic hysteresis model that combines the play model with the Cauer circuit [24,25] which takes into account power semiconductor properties [26]. By using the play model with the Cauer circuit, the hysteresis loop is described by

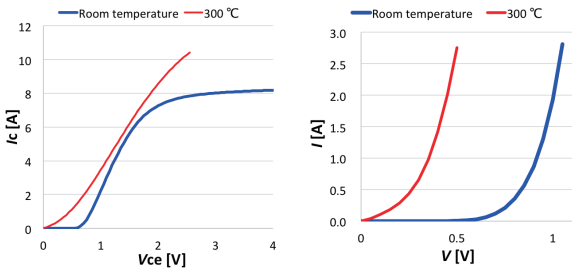

(a) (b)

Fig. 2 $I-V$ characteristics at RT and 300°C of the Si-IGBT and Si-diode measured by using SMU. (a) Si-IGBT. (b) Si-diode.

$$H_{\mathrm{AC}}(B) = H_{\mathrm{DC}}(B) + \frac{7(B^k - B^{k-1}) + 2L'h_2^{k-1}}{7R_{\mathrm{E}}\Delta t + 2L'} + \frac{3L'(h_2^k - h_2^{k-1})}{35R_{\mathrm{E}}\Delta t}, \tag{5}$$

$$H_{\mathrm{DC}}(B) = \frac{B^k}{L}, \tag{6}$$

$$R_{\mathrm{E}} = \frac{12}{\alpha\sigma d^2}, \tag{7}$$

where $H_{\mathrm{DC}}(B)$ denotes the static (DC) hysteretic property represented by the play model, L is the inductance that correspond to the magnetic permeability in the model, Δt is the time division, L' is the equivalent inductance to express the magnetic flux caused by eddy currents, k is the step number, and R_E is the resistance to represent eddy currents. Here d (=0.35 mm) is the thickness of NO sheet, σ (=1.923 × 10^6 S/m) is the electrical conductivity at RT of NO sheet, and α (= 2.14) is the anomaly factor at RT to express anomaly eddy currents[15]. Here, the parameters and DC hysteresis loops of magnetic material cores at RT are applied to the numerical simulations. In our paper, L' at f_c = 1, 4, 12, and 20 kHz is set to 3.53, 1.44, 0.558, and 0.348 mH, respectively. Here, we apply $I-V$ characteristics of the semiconductors to the current calculated from H using Eq. (2) and then can obtain numerical hysteresis curves including the power semiconductor properties. See ref. [15] for details of numerical and parameter estimation methods.

3 Results and discussion

Figures 2(a) and 2(b) show the $I-V$ characteristics at RT and 300°C of the Si-IGBT and Si-diode measured using the SMU. For the $I-V$ characteristics of Si-IGBT, the collector current I_c is measured by sweeping the collector-emitter voltage V_{ce} at V_{ge} (gate-emitter voltage) = 8 V. For the $I-V$ characteristics of Si-diode, the current is measured by sweeping the voltage at V_{ge} = 0 V. The current of the Si-IGBT and Si-diode at HT is larger than that at RT under the same voltage condition. It is assumed this is due to the fact that many carriers can overcome the barrier at HT.

Figure 3 shows the B-coil voltage V waveform of the ring specimen (shown in Fig. 1) at f_c = 20 kHz under RT and HT inverter

excitations. As shown in the magnified figure in Fig. 3, the on-voltage (almost 0 V) at 300°C is smaller than that (about 1 V) at RT because the voltage at 300°C becomes low compared to that at RT under the same current condition, as shown in Fig. 2 (See ref. [17] for details of on-voltages).

Figure 4(a) shows the experimental hysteresis curves obtained by the ring test system shown in Fig. 1. The blue and red lines correspond to curves at f_c = 20 kHz under RT and HT (300°C) inverter excitations, respectively. In the experiments, ringing noises and the slight unbalance of the semiconductor characteristics occur. The corresponding numerical hysteresis curves results are shown in Fig. 4(b). Here, by using the $I - V$ characteristics shown in Fig. 2, power semiconductor properties are taken into account in our numerical simulations. The calculated hysteresis curves are consistent with the experimental results. Here, we realize the experimental and numerical representation of the hysteretic phenomena of soft magnetic materials excited by inverter at RT and HT. The ring specimen excited by the inverter at RT and 300°C exhibits iron losses of about 81.1 and 71.6 mW/kg at f_c = 20 kHz, respectively. The trace of $\alpha \rightarrow \beta$ in the minor loop shown in Fig. 4(a) corresponds to that in voltage waveform in Fig. 3. Here, the trace of $\alpha \rightarrow \beta$ is operated in off-mode of inverter. When the inverter switches operate in off-mode, the area of the minor loops decreases with the increase of semiconductor temperature because the on-voltage at 300°C is smaller than that at RT (See refs. [15,17] for details of the minor loop in off-mode.). The iron loss under PWM inverter excitation decreases with increase of temperature of the semiconductors because the area of the minor loop under HT inverter excitation becomes small in comparison with that at RT (See ref. [15] for details of the relation between area of loop and iron loss.). Based on both experiments and numerical simulations, we for the first time found that the iron loss and hysteresis properties of magnetic materials under PWM inverter excitation depended strongly on the temperature dependence of semiconductor characteristics in not only on-mode but also off-mode.

Figure 5 shows the iron losses of the ring specimen with respect to carrier frequency under RT and HT inverter excitations. The blue and red points correspond to the iron losses of NO ring fed by inverter at RT and 300°C, respectively. The carrier frequency property of the iron loss relates to semiconductor temperature. We quantitatively evaluated the iron losses of RT magnetic materials under RT and HT (300°C) inverter excitations.

Figure 6 shows the rate of change of the iron loss η calculated from Eq. (4). Note that η at a high carrier frequency is larger than that at a low carrier frequency. η increases with increasing carrier frequency. It is considered that the number of switching times increases with the increase of carrier frequency and then the influence of the temperature dependence of the semiconductor characteristics at the high carrier frequency becomes large. Based on our coupled studies of magnetic and semiconductor

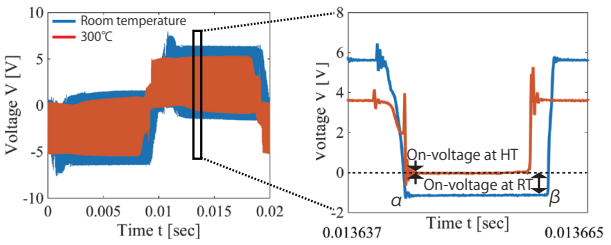

Fig. 3 Induced voltage waveforms of ring specimen (shown in Fig. 1) under RT and HT (300°C) inverter excitations at f_c = 20 kHz. Magnified figure shows on-voltages.

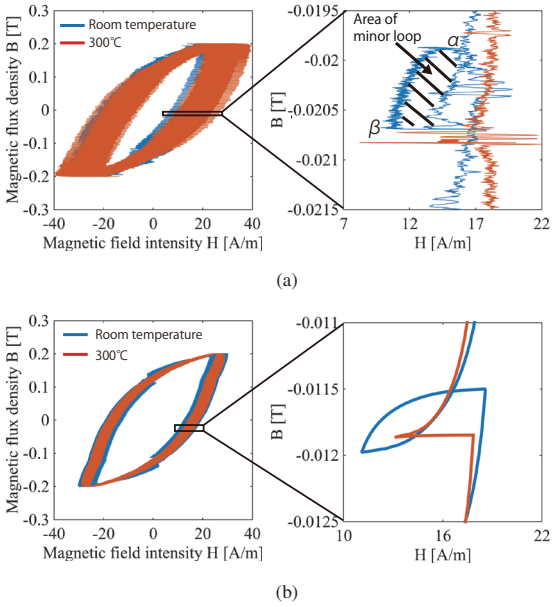

Fig. 4 (a) Experimental hysteresis curves of ring specimen (shown in Fig. 1) excited by PWM inverter at RT and 300°C. Carrier frequency was 20 kHz. Magnified figure shows the minor loop of hysteresis curves (See refs. [15,17] for more details on minor loops.). (b) Corresponding numerical hysteresis curves generated from play model with Cauer circuit.

properties, it is thought that the core losses of the HT motor system under this experimental condition can be reduced at the high carrier frequency.

Consequently, this work shows for the first time that the iron loss and hysteresis properties of magnetic materials under PWM inverter excitation depend strongly on the semiconductor temperature. These results open the way to further research in HT and high efficiency motor system based on coupled studies of magnetic and semiconductor properties. It is expected that by using our numerical simulations we can calculate the magnetic hysteretic and iron loss properties fed by HT inverters based on other new materials such as silicon carbide (SiC) and gallium nitride (GaN). In addition, since we can achieve to represent the numerical magnetic hysteretic properties under RT and HT inverter excitations, it will be possible to estimate the loss repartition (*e.g.* between the hysteresis and eddy current losses) [15,26]

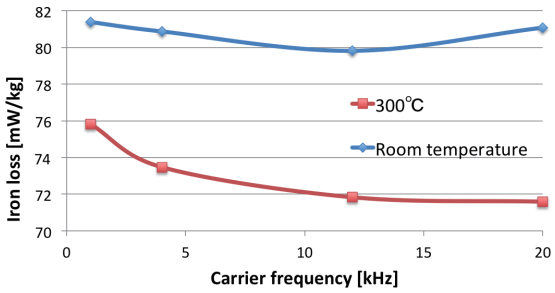

Fig. 5 Iron losses of ring specimen as function of carrier frequency at RT and 300°C. Tests were performed at carrier frequencies of 1, 4, 12, and 20 kHz.

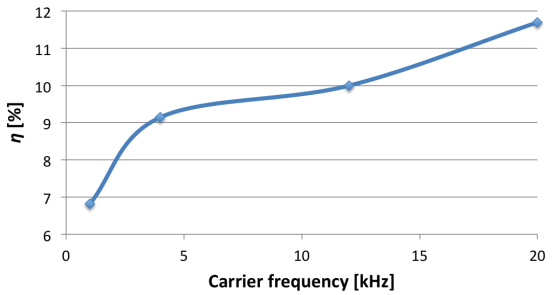

Fig. 6 Rate of change of iron loss η based on semiconductor temperature calculated by using Eq. (4).

of magnetic materials excited by inverter at RT and HT by using our numerical simulations. Also, for electrical power conversion system such as DC-DC converter (especially in high frequency applications), the semiconductor devices are used in HT environments[27]. Therefore, it is expected that our coupled studies of magnetic and semiconductor properties may be useful to reduce iron losses not only in HT motor but also in electrical power conversion system.

4 Conclusion

We experimentally and numerically examined magnetic properties of magnetic materials under RT and HT inverter excitations. We for the first time found that the iron loss and hysteresis properties of magnetic materials under PWM inverter excitation depended strongly on the temperature dependence of semiconductor characteristics. In addition, we showed that the rate of change of iron loss based on the temperature dependence of semiconductor characteristics at the high carrier frequency was larger than that at the low carrier frequency. These results open the way to further research for loss reduction of not only HT motor but also electrical power conversion system based on coupled studies of magnetic and semiconductor properties. In our future works, we will evaluate the impact of power semiconductor characteristics on iron loss properties in the driven motor and in other parameter settings. In addition, further experimental and numerical investigations are necessary under a wider range of temperatures. In future research, the iron loss and hysteresis properties of HT magnetic materials under HT inverter excitation will be addressed.

Acknowledgment This work was partly supported by the JSPS KAKENHI ♯18K13749, JST OPERA, JFE 21st Century Foundation, and the Nagamori Foundation Research Grant. We are grateful to Prof. T. Matsuda (Toyama Prefectural University) for his support in the measurement of semiconductors and Dr. S. Odawara (Kitami Institute of Technology) for fruitful discussion.

References

1) L. Burdet: Ph.D. dissertation, Citeseer, (2006).
2) T. D. Kefalas and A. G. Kladas: *IEEE Trans. on Ind. Electron.*, **61**, 4404, (2014).
3) A. Yao, A. Adachi, and K. Fujisaki: Proc. IEMDC2017, p.1 (IEEE, 2017).
4) A. Boglietti, P. Ferraris, M. Lazzari, and M. Pastorelli: *IEEE Trans. on Magn.*, **32**, 4884, (1996).
5) A. Boglietti, P. Ferraris, M. Lazzari, and F. Profumo: *IEEE Trans. on Magn.*, **27**, 5334, (1991).
6) A. Boglietti, P. Ferraris, M. Lazzari, and M. Pastorelli: *IEEE Trans. on Magn.*, **31,** , 4250, (1995).
7) M. Kawabe, T. Nomiyama, A. Shiozaki, H. Kaihara, N. Takahashi, and M. Nakano: *IEEE Trans. on Magn.*, **48,** , 3458, (2012).
8) K. Fujisaki and S. Liu: *J. Appl. Phys.*, **115**, 17A321, (2014).
9) S. Odawara, K. Fujisaki, and F. Ikeda: *IEEE Trans. on Magn.*, **50**, 1, (2014).
10) T. Taitoda, Y. Takahashi, and K. Fujiwara: *IEEE Trans. on Magn.*, **51**, 1, (2015).
11) A. Yao, K. Tsukada, S. Odawara, K. Fujisaki, Y. Shindo, N. Yoshikawa, and T. Yoshitake: *AIP Adv.*, **7**, 056618, (2017).
12) A. Yao and K. Fujisaki: Proc. LDIA2017, p.1 (IEEJ, 2017).
13) A. Yao, T. Sugimoto, S. Odawara, and K. Fujisaki: *AIP Adv.*, **8**, 056804, (2018).
14) A. Yao, T. Sugimoto, S. Odawara, and K. Fujisaki: *IEEE Trans. on Magn.*, **54**, 1, (2018).
15) A. Yao, S. Odawara, and K. Fujisaki: *IEEJ J. Ind. Appl.*, **7**, 298, (2018).
16) A. Yao, K. Tsukada, and K. Fujisaki: Proc. LDIA2017, p.1 (IEEE, 2017)
17) A. Yao, K. Tsukada, and K. Fujisaki: *IEEJ J. Ind. Appl.*, **7**, 321, (2018).
18) S. Bobbio, G. Milano, C. Serpico, and C. Visone: *IEEE Trans. on magnetics*, **33**, 4417, (1997).
19) T. Matsuo and M. Shimasaki: *IEEE Trans. on Magn.*, **41**, 3112, (2005).
20) J. Kitao, K. Hashimoto, Y. Takahashi, K. Fujiwara, Y. Ishihara, A. Ahagon, and T. Matsuo: *IEEE Trans. on Magn.*, **48**, 3375, (2012).
21) J. H. Krah: *IEEE Trans. on Magn.*, **41**, 1444, (2005).
22) Y. Shindo and O. Noro: *IEEJ Trans. on Fundamentals and Materials*, **134**, 173, (2014).
23) Y. Shindo, T. Miyazaki, and T. Matsuo: *IEEE Trans. on Magn.*, **52**, 1, (2016).
24) S. Odawara, K. Fujisaki, T. Matsuo, and Y. Shindo: *IEEJ Trans. on Ind. Appl.*, **135**, 1191, (2014).
25) T. Miyazaki, T. Mifune, T. Matsuo, Y. Shindo, Y. Takahashi, and K. Fujiwara, *J. Appl. Phys.*, **117**, 17D110, (2015).
26) S. Odawara and K. Fujisaki: *IEEE Trans. on Magn.*, **54**, 1, (2018).
27) T. Funaki, J. C. Balda, J. Junghans, A. S. Kashyap, H. A. Mantooth, F. Barlow, T. Kimoto, and T. Hikihara: *IEEE Trans. on Power electron.*, **22**, 1321, (2007).

Recieved Jan. 23, 2019; Revised Mar. 1, 2019; Accepted Mar. 9, 2019

J. Magn. Soc. Jpn., **43**, 50-58 (2019)

<Paper>

Magnetostriction Behaviors of $Fe_{100-x}Co_x$ Alloy Epitaxial Thin Films under Rotating Magnetic Field

Kana Serizawa[1,2], Mitsuru Ohtake[1], Tetsuroh Kawai[1], Masaaki Futamoto[2], Fumiyoshi Kirino[3], and Nobuyuki Inaba[4]

[1]Faculty of Engineering, Yokohama National University, *79-5 Tokiwadai, Hodogaya, Yokohama 240-8501, Japan*

[2]Faculty of Science and Engineering, Chuo University, *1-13-27 Kasuga, Bunkyo-ku, Tokyo 112-8551, Japan*

[3]Graduate School of Fine Arts, Tokyo University of the Arts, *12-8 Ueno-koen, Taito-ku, Tokyo 110-8714, Japan*

[4]Faculty of Engineering, Yamagata University, *4-3-16 Jyonan, Yonezawa, Yamagata 992-8510, Japan*

$Fe_{100-x}Co_x$ (x = 0, 30, 50 at. %) alloy thin films are prepared on MgO substrates of (001), (110), and (111) orientations by ultra-high vacuum magnetron sputtering. The influences of film orientation and composition on the magnetic anisotropy and the magnetostriction are investigated. $Fe_{100-x}Co_x$(001) single-crystal and (211) bi-crystal films are respectively obtained on MgO(001) and (110) substrates. $Fe_{100-x}Co_x$(110) films are epitaxially grown on MgO(111) substrates with two types of variants with the crystallographic orientation relationships similar to Nishiyama-Wasserman and Kurdjumov-Sachs. The (001) single-crystal and the (211) bi-crystal films, respectively, show four- and two-fold symmetric in-plane magnetic anisotropies, which are reflecting the magnetocrystalline anisotropy of $Fe_{100-x}Co_x$ crystal with the easy magnetization axes parallel to <100> or <111>. On the contrary, isotropic in-plane magnetization properties are observed for the (110) films due to an influence of the variant structure. The magnetostriction is measured under rotating magnetic field by using a cantilever method. As the Co content increases from 0 to 50 at. %, the magnetostriction coefficients, λ_{100} and λ_{111}, respectively increase from $+10^{-5}$ to $+10^{-4}$ and from -10^{-5} to $+10^{-5}$ for both $Fe_{100-x}Co_x$(001) single-crystal and (211) bi-crystal films. Large λ_{100} values are also indicated for the $Fe_{100-x}Co_x$(110) epitaxial films (x = 30, 50). The present study shows that it is possible to obtain large magnetostriction of 10^{-4} by control of the film orientation and composition.

Key words: Fe-Co alloy, epitaxial thin film, magnetostriction, rotating magnetic field

1. Introduction

Magnetic thin films with large magnetostriction coefficients have been studied for microelectromechanical-system applications such as actuators, sensors, and vibration energy harvesting devices[1–3]. RFe_2 (R: Tb, Sm, etc.) alloys show giant magnetostriction cofficients[4] of 10^{-3}. However, high external magnetic fields are required to show large magnetostriction, since they have high magnetic anisotropies. Furthermore, rare-earth free materials are desirable from the viewpoints of cost and natural resource.

Fe-Co alloys with bcc structure are typical soft magnetic materials and have recently attracted much attention as one of magnetostrictive materials, since they show large magnetostriction cofficients[5–10] of 10^{-4}. The magnetostriction behavior varies depending on the crystallographic orientation. Therefore in order to investigate the basic magnetostriction properties, it is useful to prepare epitaxial thin films, since the crystallographic orientation can be controlled by the substrate orientation. Fe-Co epitaxial films have been prepared on single-crystal substrates of GaAs[11–16], MgO[17–23], $MgAl_2O_4$[22], $SrTiO_3$[22–24], Al_2O_3[23], etc. However, the magnetostriction has not been investigated by employing Fe-Co epitaxial films, though there exist reports on the magnetostriction of polycrystalline films[8,9,25–31]. In the present study, $Fe_{100-x}Co_x$ (x = 0–50 at. %) films are prepared on MgO substrates of (001), (110), and (111) orientations. The influences of film orientation and composition on the magnetization and the magnetostriction properties are systematically investigated.

2. Experimental Procedure

An ultra-high vacuum system consisting of two chambers equipped with radio-frequency (RF) magnetron sputter deposition and reflection high-energy electron diffraction (RHEED) facilities was employed. The base pressure of deposition chamber was lower than 4×10^{-7} Pa. MgO(001), MgO(110), and Al_2O_3(0001) single-crystal substrates were used. Before film formation, substrates were heated at 600 °C in the deposition chamber to obtain clean surfaces, which were confirmed by RHEED (not shown here). MgO and $Fe_{100-x}Co_x$ alloy (x = 0, 30, 50 at. %) targets of 3 inch diameter were employed. The distance between target and substrate and the Ar gas pressure were respectively fixed at 150 mm and 0.67 Pa. The RF powers for MgO, Fe, $Fe_{70}Co_{30}$, and $Fe_{50}Co_{50}$ targets were respectively adjusted to be 200, 50, 51, and 52 W. Under these conditions, the deposition rate was 0.015 nm/s for MgO, whereas it was 0.020 nm/s for the other materials. The substrate temperature during sputter deposition was kept constant at 300 °C.

$Fe_{100-x}Co_x$ films were formed on MgO(001) and MgO(110) substrates and MgO(111) underlayers hetero-epitaxially grown on Al_2O_3(0001) substrates. The crystallographic orientation relationship between MgO underlayer and Al_2O_3 substrate was determined by RHEED as MgO(111)[$1\bar{1}0$] and (111)[$\bar{1}10$] || Al_2O_3(0001)[$1\bar{1}00$]. The MgO underlayer consisted of two (111) variants whose orientations were rotated around the film normal by 180° each other. The surface atomic arrangements of the two variants are the same. Therefore, only the crystallographic orientation of MgO(111)[$1\bar{1}0$] || Al_2O_3(0001)[$1\bar{1}00$] is used below. The thicknesses of MgO(001), MgO(110), and MgO(111)/Al_2O_3(0001) substrates were respectively 0.30, 0.30, and 0.43 mm, while that of $Fe_{100-x}Co_x$ film was fixed at 100 nm.

The crystallographic orientation relationship between film and substrate was determined by RHEED. The resulting film

Table 1 Young's moduli of Fe and MgO single crystals.

Young's modulus \ Crystal direction	<100>	<110>	<111>
E_{MgO} [GPa]	245	308	336
E_{Fe} (:= $E_{Fe_{100-x}Co_x}$) [GPa]	132	221	284

Table 2 Poisson's ratios of Fe and MgO single crystals.

Poisson's ratio \ Crystal plane & direction	MgO (001)[1$\bar{1}$0] ‖ Fe (001)[100]	MgO (001)[100] ‖ Fe (001)[110]	MgO (110)[001] ‖ Fe (211)[01$\bar{1}$]	MgO (110)[1$\bar{1}$0] ‖ Fe (211)[$\bar{1}$11]
ν_{MgO}	0.04	0.23	0.23	0.29
ν_{Fe} (:= $\nu_{Fe_{100-x}Co_x}$)	0.37	–0.05	0.18	0.23

structure was investigated by $2\theta/\omega$-scan out-of-plane and $2\theta\chi/\varphi$-scan in-plane X-ray diffractions (XRDs) with Cu-Kα radiation (wave length: 0.15418 nm). The magnetization curves were measured by vibrating sample magnetometry.

The magnetostriction was observed by using a cantilever method under a rotating magnetic field of 1.2 kOe. The bending was measured by using a laser displacement meter fixed on a vibration isolation table. The details of our measurement system are reported in our previous paper[32]. The relative length change, $\Delta l/l$, was calculated from the following formula,

$$\frac{\Delta l}{l} = \frac{\Delta S \cdot t_s^2 \cdot E_s \cdot (1+\nu_f)}{3 \cdot L^2 \cdot t_f \cdot E_f \cdot (1-\nu_s)}, \quad (1)$$

where ΔS was the measured bending, L was the distance between laser beam points (12.5 mm), t was the thickness, E was the Young's modulus, ν was the Poisson's ratio, and the subscripts of f and s respectively referred to film and substrate.

The E and the ν values of single crystal vary depending on the crystallographic direction, though E and ν are usually defined in an isotropic elastic body. In the present study, E and ν are respectively defined as $\sigma/\varepsilon_{//}$ and $-\varepsilon_{\perp}/\varepsilon_{//}$, where σ is the uniaxial stress applied along $[g_1\ g_2\ g_3]$, $\varepsilon_{//}$ is the strain occurred along $[g_1\ g_2\ g_3]$, and $\varepsilon_{\perp}$ is the strain occurred along the direction perpendicular to $[g_1\ g_2\ g_3]$ in the film plane ($[d_1\ d_2\ d_3] \perp [g_1\ g_2\ g_3] \perp$ out-of-plane direction). Based on the definitions, E and ν of cubic single crystal are respectively expressed[33,34] as

$$\frac{1}{E} = \frac{C_{11}+C_{12}}{(C_{11}-C_{12})(C_{11}+2C_{12})} + \left(\frac{1}{C_{44}} - \frac{2}{C_{11}-C_{12}}\right)(\gamma_1^2\gamma_2^2+\gamma_2^2\gamma_3^2+\gamma_3^2\gamma_1^2), \quad (2)$$

$$\nu = -\left[\frac{-C_{12}}{(C_{11}-C_{12})(C_{11}+2C_{12})} + \left(\frac{1}{C_{11}-C_{12}} - \frac{1}{2C_{44}}\right)(\gamma_1^2\delta_1^2+\gamma_2^2\delta_2^2+\gamma_3^2\delta_3^2)\right] \left[\frac{C_{11}+C_{12}}{(C_{11}-C_{12})(C_{11}+2C_{12})} + \left(\frac{1}{C_{44}} - \frac{2}{C_{11}-C_{12}}\right)(\gamma_1^2\gamma_2^2+\gamma_2^2\gamma_3^2+\gamma_3^2\gamma_1^2)\right]^{-1}, \quad (3)$$

where C_{11}, C_{12}, and C_{44} were the elastic stiffness values and

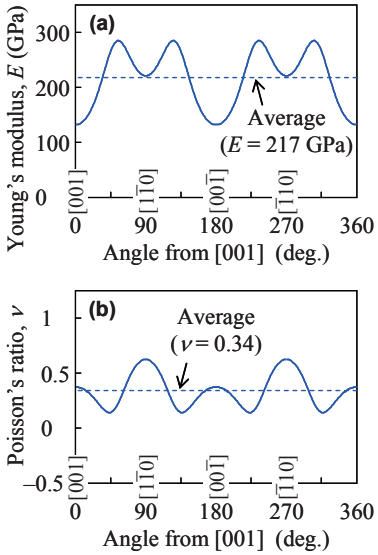

Fig. 1 In-plane (a) E and (b) ν distributions of Fe(110) single-crystal film.

(γ_1, γ_2, γ_3) and (δ_1, δ_2, δ_3) are respectively the cosines of angles of $[g_1\ g_2\ g_3]$ and $[d_1\ d_2\ d_3]$ with respect to the three crystallographic axes (a, b, c). Tables 1 and 2 summarize the E and the ν values of MgO and Fe single crystals calculated with the reported values of $(C_{11}, C_{12}, C_{44})_{MgO}$ = (286, 87, 148)[35] and $(C_{11}, C_{12}, C_{44})_{Fe}$ = (237, 141, 116)[36]. Figures 1(a) and (b), respectively, show the in-plane E and ν distributions of Fe(110) single-crystal film. The E and the ν values of Fe(110) film with multiple variants are respectively regarded as the averages of Fig. 1(a) (E = 217 GPa) and Fig. 1(b) (ν = 0.34). In the present study, the E and the ν values of Fe crystal were used in the calculation of $\Delta l/l$ for Fe-Co alloy films, since the elastic stiffness values of Fe-Co alloys were unknown. For hexagonal Al_2O_3 crystal, the reported values[37] of E = 407.5±62.5 GPa (345–470 GPa) and ν = 0.285±0.015 (0.27–0.30) were used.

3. Results and Discussion

3.1 Film growth and structure

Figures 2(a)–(c) show the RHEED patterns observed for $Fe_{100-x}Co_x$ films with different compositions formed on MgO(001), MgO(110), and MgO(111)/Al_2O_3(0001) substrates, respectively. Figures 2(d)–(f) illustrate the diffraction patterns simulated for bcc(001) single-crystal, bcc(211) bi-crystal, and bcc(110) crystal with Nishiyama-Wasserman (NW)[38,39] and Kurdumov-Sachs (KS)[40] variants, respectively. The details of the simulations have been shown in our previous papers[20–23]. The observed patterns of Figs. 2(a)–(c) are respectively in agreement with the simulated patterns of Figs. 2(d)–(f). Therefore, $Fe_{100-x}Co_x$(001) single-crystal, (211) bi-crystal, and (110) crystal films are respectively epitaxially grown on MgO(001), MgO(110), MgO(111)/Al_2O_3(0001) substrates for all the compositions of x = 0–50 at. %. The crystallographic orientation relationships are determined as

$Fe_{100-x}Co_x(001)[110]_{bcc} \parallel MgO(001)[100]$,

$Fe_{100-x}Co_x(211)[01\bar{1}]_{bcc} \parallel MgO(110)[001]$, (type A)

$Fe_{100-x}Co_x(211)[0\bar{1}1]_{bcc} \parallel MgO(110)[001]$, (type B)

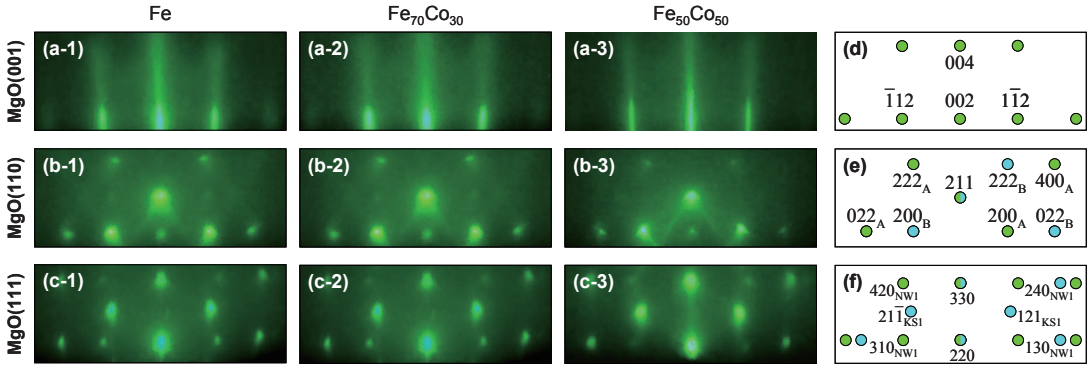

Fig. 2 (a)–(c) RHEED patterns observed for (a-1)–(c-1) Fe, (a-2)–(c-2) $Fe_{70}Co_{30}$, and (a-3)–(c-3) $Fe_{50}Co_{50}$ films formed on (a) MgO(001), (b) MgO(110), and (c) MgO(111)/Al_2O_3(0001) substrates. (d)–(f) Schematic diagrams of RHEED patterns simulated for (d) bcc(001) single-crystal, (e) bcc(211) bi-crystal, and (f) bcc(110) multi-crystal with NW and KS variants. The incident electron beam is parallel to (a) MgO[100], (b) MgO[001], (c) MgO[1$\bar{1}$0], (d) bcc[110], (e) bcc[01$\bar{1}$]+[0$\bar{1}$1], or (f) bcc[001]+[1$\bar{1}$1].

$Fe_{100-x}Co_x(110)[001]_{bcc} \parallel MgO(111)[1\bar{1}0]$, (type NW1)
$Fe_{100-x}Co_x(110)[001]_{bcc} \parallel MgO(111)[01\bar{1}]$, (type NW2)
$Fe_{100-x}Co_x(110)[001]_{bcc} \parallel MgO(111)[\bar{1}01]$, (type NW3)
$Fe_{100-x}Co_x(110)[1\bar{1}1]_{bcc} \parallel MgO(111)[1\bar{1}0]$, (type KS1)
$Fe_{100-x}Co_x(110)[1\bar{1}1]_{bcc} \parallel MgO(111)[0\bar{1}1]$, (type KS2)
$Fe_{100-x}Co_x(110)[1\bar{1}1]_{bcc} \parallel MgO(111)[\bar{1}01]$, (type KS3)
$Fe_{100-x}Co_x(110)[\bar{1}1\bar{1}]_{bcc} \parallel MgO(111)[1\bar{1}0]$, (type KS4)
$Fe_{100-x}Co_x(110)[\bar{1}1\bar{1}]_{bcc} \parallel MgO(111)[0\bar{1}1]$, (type KS5)
$Fe_{100-x}Co_x(110)[\bar{1}1\bar{1}]_{bcc} \parallel MgO(111)[\bar{1}01]$, (type KS6)

which are similar to the case of $Fe_{100-x}Co_x$ film growth by molecular beam epitaxy[20–23].

Figures 3(a-1)–(c-1) show the out-of-plane XRD patterns of the $Fe_{100-x}Co_x$ epitaxial films with different orientations. bcc(002), bcc(211), and bcc(110) reflections are observed for the films formed on MgO(001), MgO(110), and MgO(111)/Al_2O_3(0001) substrates, respectively. Figures 3(a-2)–(c-2) show the in-plane XRD patterns of the epitaxial films formed on MgO(001), MgO(110), and MgO(111)/Al_2O_3(0001) substrates measured by making the scattering vector parallel to MgO[1$\bar{1}$0], MgO[001], and MgO[1$\bar{1}$0] ($\parallel$ Al_2O_3[1$\bar{1}$00]), respectively. bcc(200) reflection is observed in the patterns of $Fe_{100-x}Co_x$(001) single-crystal films [Fig. 3(a-2)]. bcc(01$\bar{1}$) reflection from the A-type variant and bcc(0$\bar{1}$1) reflection from the B-type variant

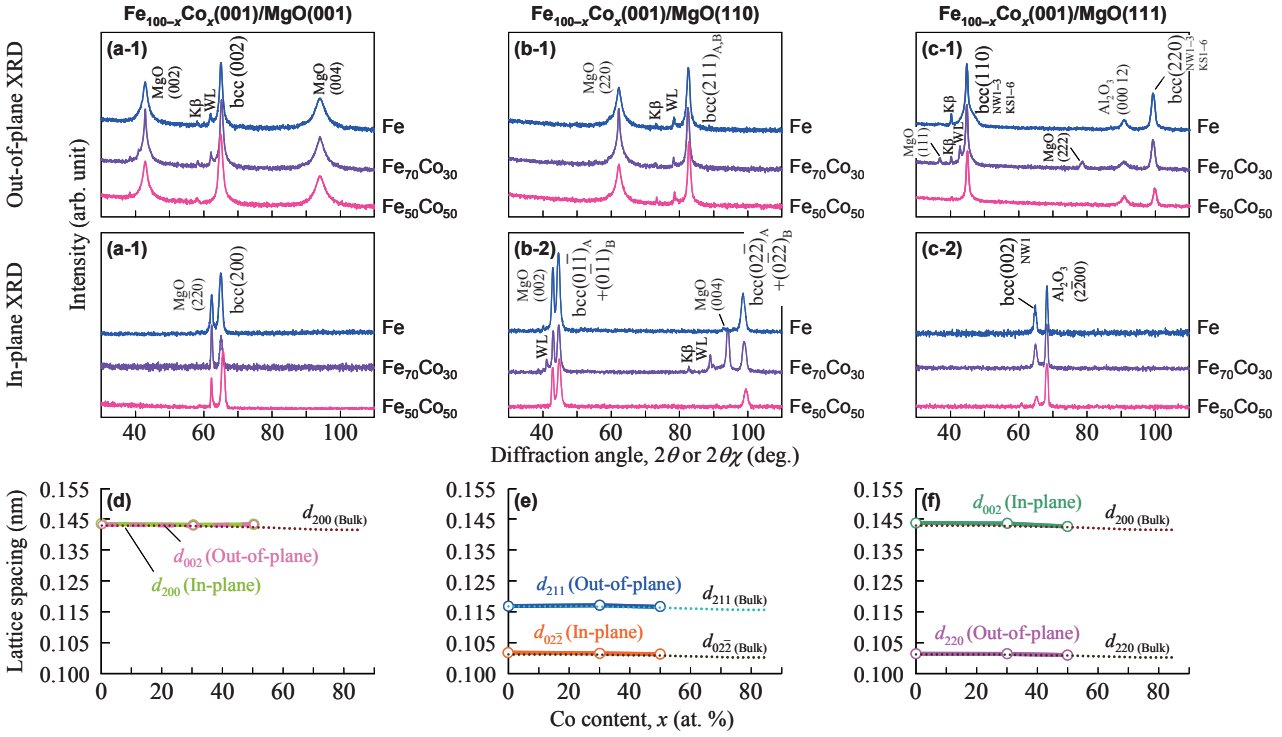

Fig. 3 (a-1)–(c-1) Out-of-plane and (a-2)–(c-2) in-plane XRD patterns of Fe, $Fe_{70}Co_{30}$, and $Fe_{50}Co_{50}$ films formed on (a) MgO(001), (b) MgO(110), and (c) MgO(111)/Al_2O_3(0001) substrates. The scattering vector of in-plane XRD is parallel to (a-2) MgO[1$\bar{1}$0], (b-2) MgO[001], or (c-2) MgO[1$\bar{1}$0] ($\parallel$ Al_2O_3[1$\bar{1}$00]). The intensity is shown in logarithmic scale. (d)–(f) Compositional dependences of out-of-plane and in-plane lattice spacings of $Fe_{100-x}Co_x$ films formed on (d) MgO(001), (e) MgO(110), and (f) MgO(111)/Al_2O_3(0001) substrates.

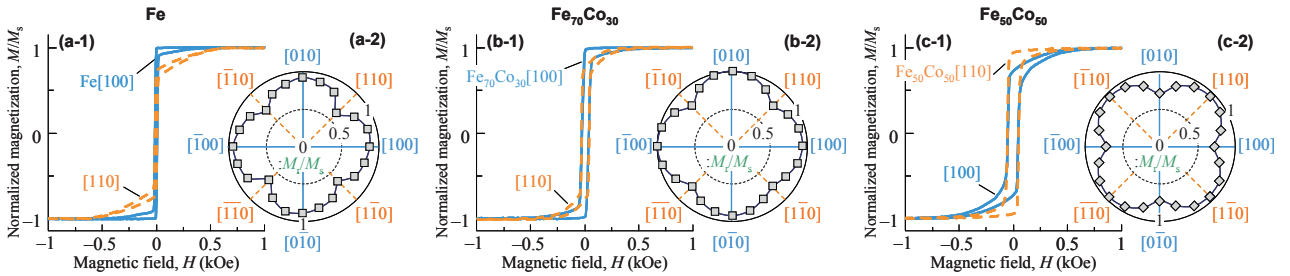

Fig. 4 (a-1)–(c-1) In-plane magnetization curves and (a-2)–(c-2) M_r/M_s distributions measured for (a) Fe, (b) $Fe_{70}Co_{30}$, and (c) $Fe_{50}Co_{50}$(001) single-crystal films formed on MgO(001) substrates. The applied magnetic field directions are shown by using the crystallographic directions of $Fe_{100-x}Co_x$ film.

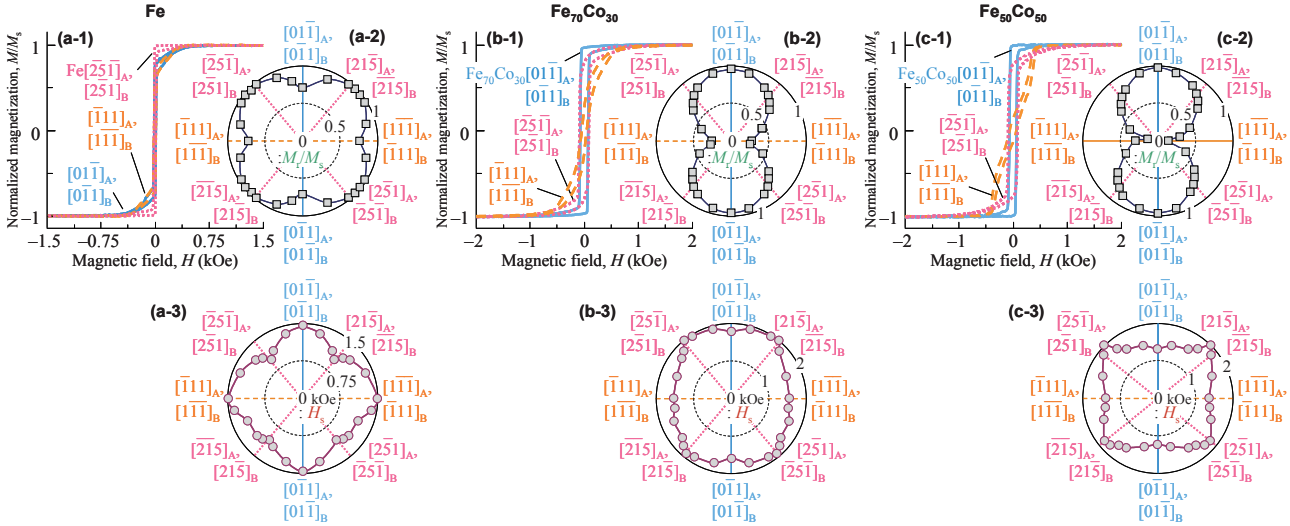

Fig. 5 (a-1)–(c-1) In-plane magnetization curves and (a-2)–(c-2) M_r/M_s and (a-3)–(c-3) H_s distributions measured for (a) Fe, (b) $Fe_{70}Co_{30}$, and (c) $Fe_{50}Co_{50}$(211) bi-crystal films formed on MgO(110) substrates. The applied magnetic field directions are shown by using the crystallographic directions of two $Fe_{100-x}Co_x$(211) variants.

seem to be overlapped around $2\theta\chi = 45°$ in the patterns of $Fe_{100-x}Co_x$(211) bi-crystal films [Fig. 3(b-2)] by considering the epitaxial orientation relationships determined by RHEED. bcc(002) reflection from the NW1-type variant is recognized, whereas bcc($1\bar{1}1$) reflection from the KS1-type variant and bcc($\bar{1}1\bar{1}$) reflection from the KS4-type variant, which are expected to appear around $2\theta\chi = 55°$, are absent in the patterns of $Fe_{100-x}Co_x$(110) epitaxial films [Fig. 3(c-2)], because the bcc(*hkl*) reflections (h, k, l = ±1) are forbidden. The out-of-plane and in-plane XRDs confirm the epitaxial orientation relationships determined by RHEED. Figures 3(d)–(f) summarize the out-of-plane and in-plane lattice spacings of $Fe_{100-x}Co_x$ films, which are estimated from the XRD data. The lattice parameters of $Fe_{100-x}Co_x$ films agree with small differences within ±0.7% with those of bulk $Fe_{100-x}Co_x$ crystal[41], which indicates that the lattice strains of $Fe_{100-x}Co_x$ films are small.

3.2 Magnetic anisotropy

Figures 4(a-1) and (b-1) show two typical examples of in-plane magnetization curves measured for the Fe and the $Fe_{70}Co_{30}$(001) single-crystal films. The distributions of normalized remnant magnetization, M_r/M_s, are summarized in Figs. 4(a-2) and (b-2). The applied magnetic field directions are shown by using the crystallographic directions of $Fe_{100-x}Co_x$ film. The films show four-fold symmetric in-plane magnetic anisotropies. The easy magnetization directions are observed along [100], [010], [$\bar{1}$00], and [0$\bar{1}$0] (blue solid lines in Figs. 4(a-2) and (b-2)), which is reflecting the magnetocrystalline anisotropy of $Fe_{100-x}Co_x$ crystal with the easy magnetization axes parallel to <100>[6]. Figure 4(c) shows the magnetization property of the $Fe_{50}Co_{50}$(001) single-crystal film. Although a four-fold symmetry in in-plane magnetic anisotropy is recognized, the easy magnetization directions are parallel to [110], [$\bar{1}$10], [$\bar{1}\bar{1}$0], and [1$\bar{1}$0] (orange dotted lines in Fig. 4(c-2)), which are different with those observed for Fe and $Fe_{70}Co_{30}$ films. It is known that the easy magnetization axes of bulk $Fe_{100-x}Co_x$ crystal vary from <100> to <111> when the Co content increases beyond about 40 at. %[6]. Therefore, the in-plane magnetic anisotropy observed for $Fe_{50}Co_{50}$ film seems to be reflecting the magnetocrystalline anisotropy of $Fe_{100-x}Co_x$ crystal with the easy axes parallel to <111> and the demagnetization field. The magnetic anisotropy of $Fe_{100-x}Co_x$(001) film varies depending on the composition, similar to the case of bulk crystal.

Figure 5(a-1) shows the hysteresis curves of the Fe(211) bi-crystal film. The distributions of M_r/M_s and saturation field (H_s) are respectively summarized in Figs. 5(a-2) and (a-3). The applied field directions are shown by using the crystallographic directions of two (211) variants. The Fe film shows a two-fold

symmetric in-plane magnetic anisotropy. The easy magnetization directions are observed along $[\bar{2}5\bar{1}]_A$, $[\bar{2}1\bar{5}]_A$, $[\bar{2}5\bar{1}]_B$, and $[\bar{2}1\bar{5}]_B$ (pink dotted lines in Figs. 5(a-2) and (a-3)), which are respectively obtained by projecting $[010]_A$, $[001]_A$, $[010]_B$, and $[001]_B$ on the (211) surface as shown in Fig. 6. Therefore, the magnetic anisotropy is interpreted to be reflecting the magnetocrystalline anisotropy of $Fe_{100-x}Co_x$ crystal with the easy axes parallel to <100> and the demagnetization film, similar to the cases of Fe and $Fe_{70}Co_{30}$(001) single-crystal films. Figure 5(c) shows the magnetic property of the $Fe_{50}Co_{50}$(211) film. A two-fold symmetry in in-plane magnetic anisotropy is observed. However, the easy magnetization directions are parallel to $[01\bar{1}]_A$+$[0\bar{1}1]_B$ and $[0\bar{1}1]_A$+$[01\bar{1}]_B$ (blue solid lines in Figs. 5(c-2) and (c-3)). It is also noted that the H_s values measured along $[\bar{1}11]_A$+$[1\bar{1}\bar{1}]_B$ and $[1\bar{1}\bar{1}]_A$+$[\bar{1}11]_B$ are not so high (orange dotted lines in Fig. 5(c-3)), though the M_r/M_s values are low (orange dotted lines in Fig. 5(c-2)). Therefore, the film is moderately easily magnetized along $[\bar{1}11]_A$+$[1\bar{1}\bar{1}]_B$ and $[1\bar{1}\bar{1}]_A$+$[\bar{1}11]_B$. On the contrary, the magnetization curves measured along $[\bar{2}5\bar{1}]_A$, $[\bar{2}1\bar{5}]_A$, $[\bar{2}5\bar{1}]_B$, and $[\bar{2}1\bar{5}]_B$, which are respectively obtained by projecting $[010]_A$, $[001]_A$, $[010]_B$, and $[001]_B$ on the film plane, saturate at higher magnetic fields (pink dotted lines in Fig. 5(c-3)). When the Co content increases up to 50 at. %, the easy and the hard magnetization axes are respectively considered to be parallel to <111> and <100>[6]. Therefore, the $Fe_{50}Co_{50}$(211) film shows the in-plane magnetic anisotropy reflecting the magnetocrystalline anisotropy of $Fe_{100-x}Co_x$ crystal with the easy magnetization axes parallel to <111> and the demagnetization field. Figure 5(b) shows the magnetization property of the $Fe_{70}Co_{30}$(211) film. The M_r/M_s and the H_s distributions of $Fe_{70}Co_{30}$ film are similar to those of $Fe_{50}Co_{50}$ film. The result suggests that the $Fe_{70}Co_{30}$ film also has easy magnetization axes parallel to <111>, though the easy axes of bulk $Fe_{70}Co_{30}$ crystal are parallel to <100>[6]. The threshold composition where the easy magnetization axes change from <100> to <111> seems to be delicately influenced by the film orientation.

Figure 7 shows the in-plane magnetic properties of the $Fe_{100-x}Co_x$(110) epitaxial films with NW and KS variants formed on MgO(111)/Al_2O_3(0001) substrates. The films show almost isotropic magnetization properties. Nine (110) variants are coexisting in the (110) epitaxial films and the respective magnetic anisotropies are overlapped. Therefore, isotropic magnetization properties are considered to be observed.

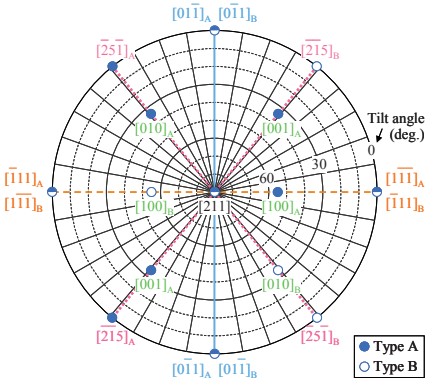

Fig. 6 Pole-figure map of an bcc(211) bi-crystalline film showing the angles of typical crystallographic directions.

3.3 Magnetostriction of (001) single-crystal films

The relative length change, $\Delta l/l$, of a cubic crystal caused by magnetostriction[8] is shown as

$$\frac{\Delta l}{l} = \frac{3}{2}\lambda_{100}\left(\alpha_1^2\beta_1^2 + \alpha_2^2\beta_2^2 + \alpha_3^2\beta_3^2 - \frac{1}{3}\right) + 3\lambda_{111}\left(\alpha_1\alpha_2\beta_1\beta_2 + \alpha_2\alpha_3\beta_2\beta_3 + \alpha_3\alpha_1\beta_3\beta_1\right), \quad (4)$$

where λ_{100} and λ_{111} are the magnetostriction coefficients, (α_1, α_2, α_3) and (β_1, β_2, β_3) are respectively the cosines of the angles of magnetization and observation directions with respect to the three crystallographic axes (a, b, c).

When the magnetization rotates in a (001) plane under in-plane rotating magnetic field as shown in Fig. 8(a), the crystallographic direction of magnetization is shown as [cosφ sinφ 0], where φ is the angle of magnetization direction with respect to [100]. The (α_1, α_2, α_3) values are thus expressed as

$$(\alpha_1, \alpha_2, \alpha_3)_{(001)} = (\cos\varphi, \sin\varphi, 0). \quad (5)$$

When the observation directions are parallel to [100] and [110], the $(\beta_1, \beta_2, \beta_3)_{[100]}$ and the $(\beta_1, \beta_2, \beta_3)_{[110]}$ values are respectively expressed as

$$(\beta_1, \beta_2, \beta_3)_{[001]} = (1, 0, 0), \quad (6)$$

$$(\beta_1, \beta_2, \beta_3)_{[110]} = \left(0, \frac{1}{\sqrt{2}}, \frac{1}{\sqrt{2}}\right). \quad (7)$$

By substituting Eqs. (5)–(7) into (4), the relative length changes measured along [100] and [110] under in-plane rotating

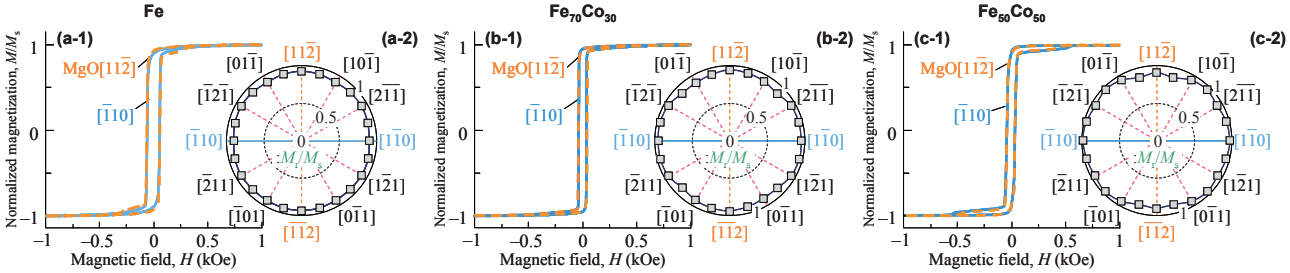

Fig. 7 (a-1)–(c-1) In-plane magnetization curves and (a-2)–(c-2) M_r/M_s distributions measured for (a) Fe, (b) $Fe_{70}Co_{30}$, and (c) $Fe_{50}Co_{50}$(110) epitaxial films with NW and KS variants formed on MgO(111)/Al_2O_3(0001) substrates. The applied magnetic field directions are shown by using the crystallographic directions of MgO underlayer.

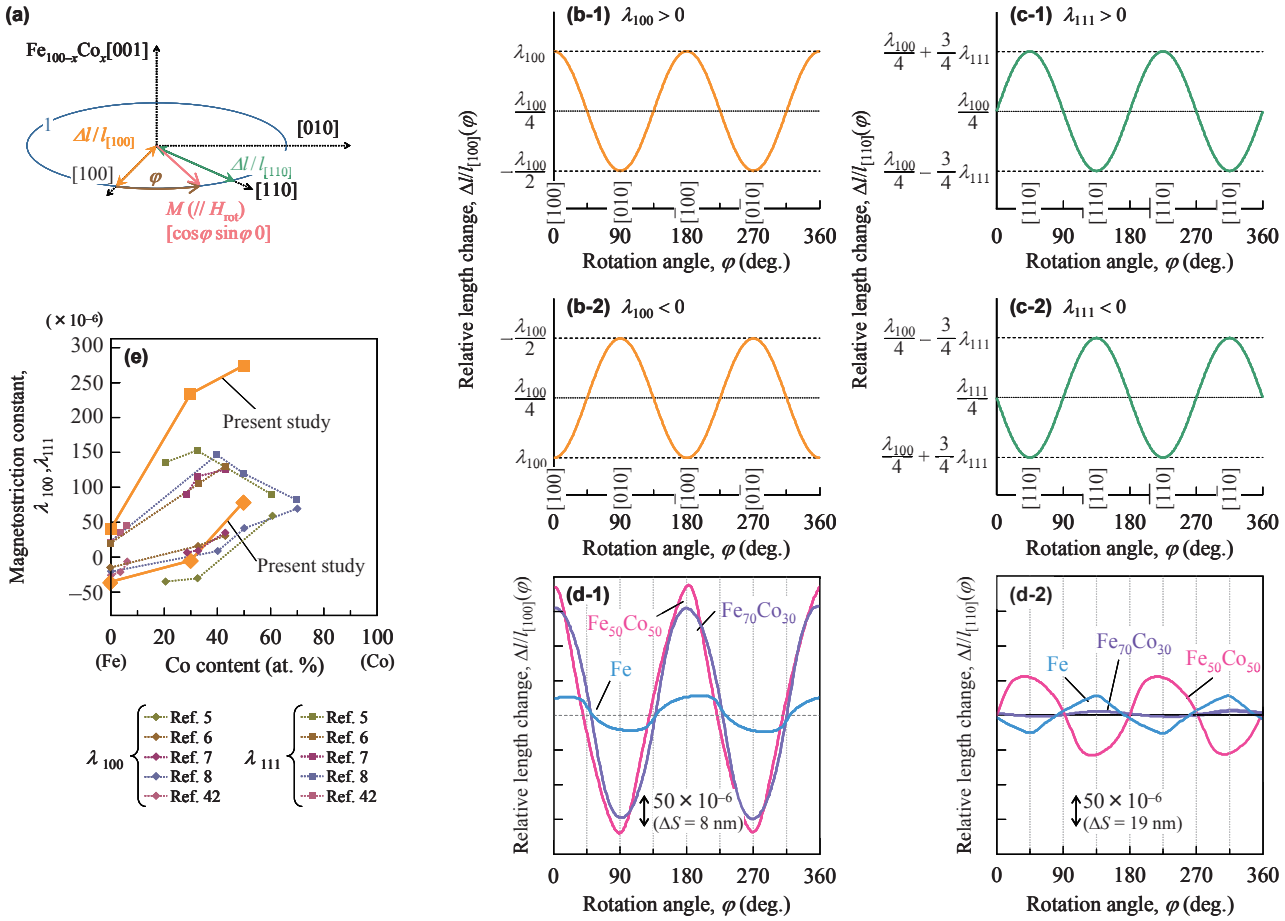

Fig. 8 (a) Schematic diagram showing the magnetization and the observation directions with respect to the typical crystallographic directions. (b) $\Delta l/l_{[100]}(\varphi)$ and (c) $\Delta l/l_{[110]}(\varphi)$ calculated for (001) single-crystal films with (b-1) $\lambda_{100} > 0$, (b-2) $\lambda_{100} < 0$, (c-1) $\lambda_{111} > 0$, and (c-2) $\lambda_{111} < 0$. (d-1) $\Delta l/l_{[100]}(\varphi)$ and (d-2) $\Delta l/l_{[110]}(\varphi)$ measured for $Fe_{100-x}Co_x(001)$ single-crystal films formed on MgO(001) substrates. (e) Compositional dependences of λ_{100} and λ_{111}. The bulk values in (e) are cited from Refs. 5–8 and 42.

magnetic field, $\Delta l/l_{[100]}(\varphi)$ and $\Delta l/l_{[110]}(\varphi)$, are given as

$$\frac{\Delta l}{l_{[100]}}(\varphi) = \frac{3}{4}\lambda_{100}\cos 2\varphi + \frac{1}{4}\lambda_{100}, \tag{8}$$

$$\frac{\Delta l}{l_{[110]}}(\varphi) = \frac{3}{4}\lambda_{111}\sin 2\varphi + \frac{1}{4}\lambda_{100}, \tag{9}$$

which are respectively cosine and sine waves. It is noted that the phases of $\Delta l/l_{[100]}(\varphi)$ and $\Delta l/l_{[110]}(\varphi)$, respectively, reverse depending on the signs of λ_{100} and λ_{111}, as shown in Figs. 8(b) and (c). Furthermore, the λ_{100} and the λ_{111} values can be estimated by using the following relations,

$$\lambda_{100} = \frac{4}{3}\left[\frac{\Delta l}{l_{[100]}}(\varphi = 0°) - \frac{\Delta l}{l_{[100]}}(\varphi = 45°)\right], \tag{10}$$

$$\lambda_{111} = \frac{4}{3}\left[\frac{\Delta l}{l_{[110]}}(\varphi = 45°) - \frac{\Delta l}{l_{[110]}}(\varphi = 90°)\right]. \tag{11}$$

Figure 8(d-1) shows the $\Delta l/l_{[100]}(\varphi)$ measured for the $Fe_{100-x}Co_x(001)$ single-crystal films with different compositions. The phases of observed waves are in agreement with that of calculated wave of Fig. 8(b-1). The λ_{100} value is thus positive for all the $Fe_{100-x}Co_x(001)$ films. Figure 8(d-2) shows the $\Delta l/l_{[110]}(\varphi)$ measured for the $Fe_{100-x}Co_x(001)$ films. The phases of waves observed for Fe and $Fe_{70}Co_{30}$ films agree with that of calculated wave of Fig. 8(c-2), whereas the phase of wave observed for $Fe_{50}Co_{50}$ film is in agreement with that of wave of Fig. 8(c-1). Therefore, the λ_{111} value is negative for the Fe and the $Fe_{70}Co_{30}$ films, while that is positive for the $Fe_{50}Co_{50}$ film.

Figure 8(e) shows the λ_{100} and the λ_{111} values plotted as a function of Co content. The λ_{100} and the λ_{111} values increase with increasing the Co content. The $Fe_{70}Co_{30}$ film shows a large λ_{100} value of $+234\times10^{-6}$ and a small λ_{111} value of -5×10^{-6}. On the contrary, a large λ_{100} value of $+274\times10^{-6}$ and a moderately large λ_{111} value of $+78\times10^{-6}$ are observed for the $Fe_{50}Co_{50}$ film.

3.4 Magnetostriction of (211) bi-crystal films

When the magnetization rotates in a $(211)_A$ plane as shown in Fig. 9(a), the crystallographic direction of magnetization is shown as $[-\sin\chi/\sqrt{3}\ \ \cos\chi/\sqrt{2}+\sin\chi/\sqrt{3}\ \ -\cos\chi/\sqrt{2}+\sin\chi/\sqrt{3}]$, where χ is the angle of magnetization direction with respect to $[01\bar{1}]_A$ ($\|$ MgO[001]). The $(\alpha_1, \alpha_2, \alpha_3)_{(211)A}$ values are thus expressed as

$$(\alpha_1, \alpha_2, \alpha_3)_{(211)A} = \left(-\frac{\sin\chi}{\sqrt{3}},\ \frac{\cos\chi}{\sqrt{2}}+\frac{\sin\chi}{\sqrt{3}},\ -\frac{\cos\chi}{\sqrt{2}}+\frac{\sin\chi}{\sqrt{3}}\right). \tag{12}$$

When the observation directions are parallel to $[01\bar{1}]_A$ and $[\bar{1}11]_A$, the $(\beta_1, \beta_2, \beta_3)_{[01\bar{1}]A}$ and the $(\beta_1, \beta_2, \beta_3)_{[\bar{1}11]A}$ values are respectively expressed as

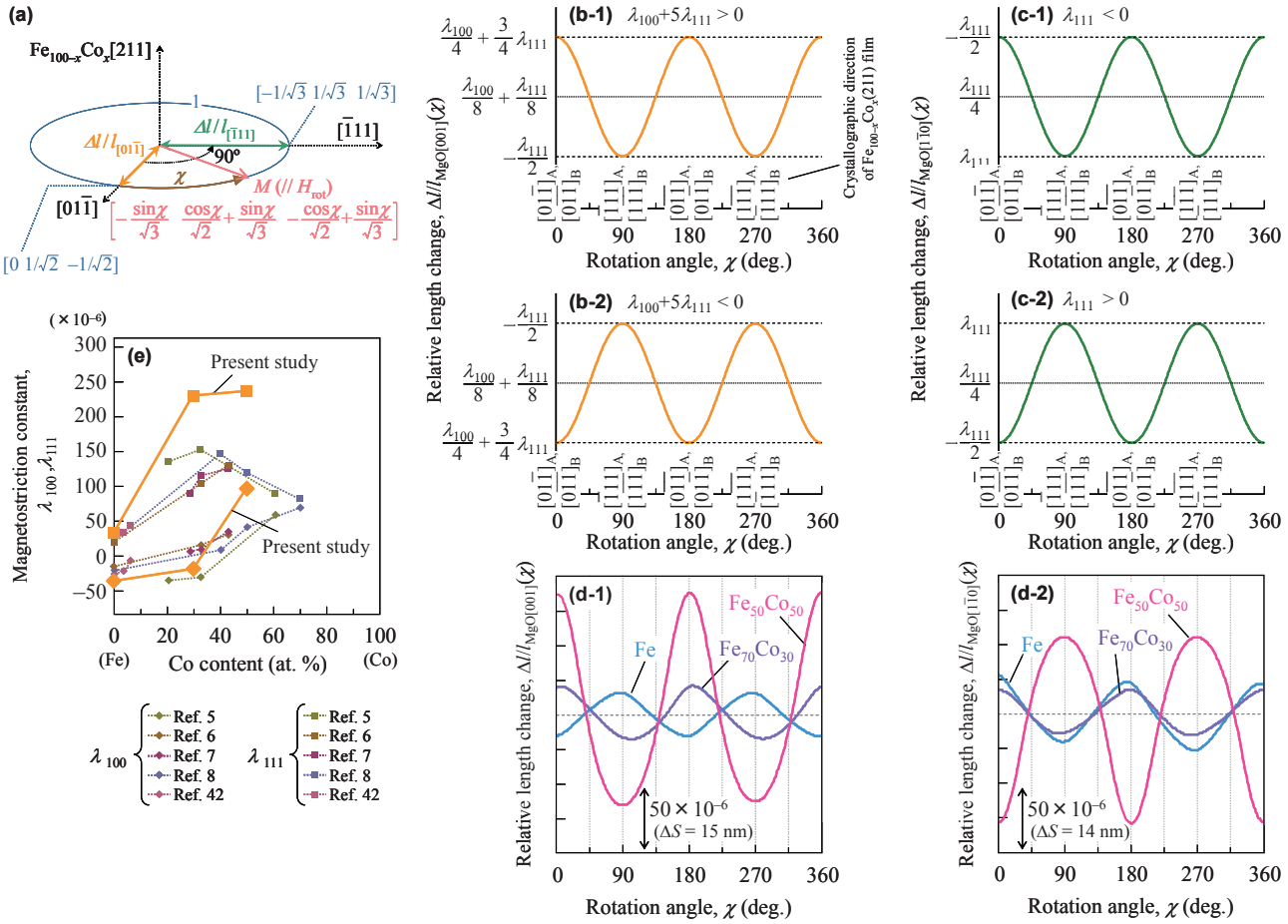

Fig. 9 (a) Schematic diagram showing the magnetization and the observation directions with respect to the typical crystallographic directions. (b) $\Delta l//l_{MgO[001]}(\varphi)$ and (c) $\Delta l//l_{MgO[1\bar{1}0]}(\varphi)$ calculated for (211) bi-crystal films with (b-1) $\lambda_{100}+5\lambda_{111} > 0$, (b-2) $\lambda_{100}+5\lambda_{111} < 0$, (c-1) $\lambda_{111} < 0$, and (c-2) $\lambda_{111} > 0$. (d-1) $\Delta l//l_{MgO[001]}(\varphi)$ and (d-2) $\Delta l//l_{MgO[1\bar{1}0]}(\varphi)$ measured for $Fe_{100-x}Co_x$(211) bi-crystal films formed on MgO(110) substrates. (e) Compositional dependences of λ_{100} and λ_{111}. The bulk values in (e) are cited from Refs. 5–8 and 42.

$$(\beta_1, \beta_2, \beta_3)_{[01\bar{1}]A} = (0, \frac{1}{\sqrt{2}}, -\frac{1}{\sqrt{2}}), \tag{13}$$

$$(\beta_1, \beta_2, \beta_3)_{[\bar{1}11]A} = (-\frac{1}{\sqrt{2}}, \frac{1}{\sqrt{3}}, \frac{1}{\sqrt{3}}). \tag{14}$$

By substituting Eqs. (12)–(14) into (4), the $\Delta l//l_{[01\bar{1}]A}(\chi)$ and the $\Delta l//l_{[\bar{1}11]A}(\chi)$ are respectively given as

$$\frac{\Delta l}{l_{[01\bar{1}]A}}(\chi) = \left(\frac{1}{8}\lambda_{100} + \frac{5}{8}\lambda_{111}\right)\cos 2\chi + \left(\frac{1}{8}\lambda_{100} + \frac{1}{8}\lambda_{111}\right), \tag{15}$$

$$\frac{\Delta l}{l_{[\bar{1}11]A}}(\chi) = -\frac{3}{4}\lambda_{111}\cos 2\chi + \frac{1}{4}\lambda_{111}. \tag{16}$$

Since the $Fe_{100-x}Co_x$(211) films consist of two types of variants, A and B, it is necessary to take into account the $\Delta l//l_{[0\bar{1}1]B}(\chi)$ and the $\Delta l//l_{[1\bar{1}\bar{1}]B}(\chi)$, which are respectively shown as follows,

$$\frac{\Delta l}{l_{[0\bar{1}1]B}}(\chi) = \left(\frac{1}{8}\lambda_{100} + \frac{5}{8}\lambda_{111}\right)\cos 2\chi + \left(\frac{1}{8}\lambda_{100} + \frac{1}{8}\lambda_{111}\right), \tag{17}$$

$$\frac{\Delta l}{l_{[1\bar{1}\bar{1}]B}}(\chi) = -\frac{3}{4}\lambda_{111}\cos 2\chi + \frac{1}{4}\lambda_{111}. \tag{18}$$

Therefore, when the magnetostriction is measured along MgO[001] (|| $Fe_{100-x}Co_x[0\,1\,\bar{1}]_A$+$[0\,\bar{1}\,1]_B$) and MgO[1 $\bar{1}$ 0] (|| $Fe_{100-x}Co_x[\bar{1}\,1\,1]_A$+$[1\,\bar{1}\,\bar{1}]_B$), the averages of relative length changes of types A and B variants, $\Delta l//l_{MgO[001]}(\chi)$ and $\Delta l//l_{MgO[1\bar{1}0]}(\chi)$, are respectively given as

$$\frac{\Delta l}{l_{MgO[001]}}(\chi) = \frac{1}{2}\left[\frac{\Delta l}{l_{[01\bar{1}]A}}(\chi) + \frac{\Delta l}{l_{[0\bar{1}1]B}}(\chi)\right] = \left(\frac{1}{8}\lambda_{100} + \frac{5}{8}\lambda_{111}\right)\cos 2\chi + \left(\frac{1}{8}\lambda_{100} + \frac{1}{8}\lambda_{111}\right), \tag{19}$$

$$\frac{\Delta l}{l_{MgO[1\bar{1}0]}}(\chi) = \frac{1}{2}\left[\frac{\Delta l}{l_{[\bar{1}11]A}}(\chi) + \frac{\Delta l}{l_{[1\bar{1}\bar{1}]B}}(\chi)\right] = -\frac{3}{4}\lambda_{111}\cos 2\chi + \frac{1}{4}\lambda_{111}, \tag{20}$$

which are shown in Figs. 9(b) and (c). Furthermore, the λ_{100} and the λ_{111} values can be estimated by using the following equations,

$$\lambda_{100} = 8\left[\frac{\Delta l}{l_{MgO[001]}}(\chi = 0°) - \frac{\Delta l}{l_{MgO[001]}}(\chi = 45°)\right] + \frac{20}{3}\left[\frac{\Delta l}{l_{MgO[1\bar{1}0]}}(\chi = 90°) - \frac{\Delta l}{l_{MgO[1\bar{1}0]}}(\chi = 135°)\right], \tag{21}$$

$$\lambda_{111} = -\frac{4}{3}\left[\frac{\Delta l}{l_{MgO[1\bar{1}0]}}(\chi = 90°) - \frac{\Delta l}{l_{MgO[1\bar{1}0]}}(\chi = 135°)\right]. \tag{22}$$

Figure 9(d) shows the $\Delta l//l_{MgO[001]}(\chi)$ and the $\Delta l//l_{MgO[1\bar{1}0]}(\chi)$ measured for the $Fe_{100-x}Co_x(211)$ films. Figure 9(e) summarizes the λ_{100} and the λ_{111} values. As the Co content increases, the λ_{100} and the λ_{111} values increase, similar to the case of $Fe_{100-x}Co_x(001)$ single-crystal film. The $Fe_{50}Co_{50}(211)$ film shows a large λ_{100} value of $+236\times10^{-6}$ and a moderately large λ_{111} value of $+97\times10^{-6}$.

3.5 Magnetostriction of $Fe_{100-x}Co_x(110)$ epitaxial films with NW and KS variants

When the magnetization rotates in a (110) plane as shown in Fig. 10(a), the crystallographic direction of magnetization is shown as $[\sin\psi/\sqrt{2}\ \ -\sin\psi/\sqrt{2}\ \ \cos\psi]$. Here, ψ is the angle of magnetization direction with respect to [001]. The $(\alpha_1, \alpha_2, \alpha_3)$ values are thus expressed as

$$(\alpha_1, \alpha_2, \alpha_3) = (\sin\psi/\sqrt{2}, -\sin\psi/\sqrt{2}, \cos\psi). \tag{23}$$

When the angle of in-plane observation direction with respect to [001] is shown as ω, the $(\beta_1, \beta_2, \beta_3)$ values are expressed as

$$(\beta_1, \beta_2, \beta_3) = (\sin\omega/\sqrt{2}, -\sin\omega/\sqrt{2}, \cos\omega). \tag{24}$$

The $\Delta l//l_{[\sin\omega/\sqrt{2}\ -\sin\omega/\sqrt{2}\ \cos\omega]}$ is thus given by substituting Eqs. (23) and (24) into (4) as follows,

$$\frac{\Delta l}{l}(\psi,\omega)_{[\sin\omega/\sqrt{2}\ -\sin\omega/\sqrt{2}\ \cos\omega]} = \frac{2}{3}\lambda_{100}\left(\frac{\sin^2\psi\sin^2\omega}{2} + \cos^2\psi\cos^2\omega - \frac{1}{3}\right) + 3\lambda_{100}\left(\frac{\sin^2\psi\sin^2\omega}{4} + \sin\psi\cos\psi\sin\omega\cos\omega\right) \tag{25}$$

In order to characterize the magnetostriction of an epitaxial film with multi-variant structure, it is necessary to take into account the volume ratio of each variant and the respective relative length changes. However, there are as many as 9 variants in the $Fe_{100-x}Co_x(110)$ epitaxial films prepared in the present study. Therefore, the in-plane orientation can be regarded as being random and the average of $\Delta l/l(\psi)$ of each variant is expressed as

$$\overline{\frac{\Delta l}{l}(\psi)} = \frac{1}{2\pi}\int_0^{2\pi}\frac{\Delta l}{l}(\psi,\omega)_{[\sin\omega/\sqrt{2}\ -\sin\omega/\sqrt{2}\ \cos\omega]}\,d\omega = \frac{3}{16}\left(\lambda_{100}-\lambda_{111}\right)\cos2\psi + \frac{1}{16}\left(\lambda_{100}+3\lambda_{111}\right), \tag{26}$$

which is shown in Fig. 10(b). Although the relationship of $\lambda_{100} > \lambda_{111}$, $\lambda_{100} = \lambda_{111}$, or $\lambda_{100} < \lambda_{111}$ can be determined by considering the phase of observed wave, the values of λ_{100} and λ_{111} can not be estimated in the case of the $Fe_{100-x}Co_x(110)$ epitaxial film. The $(\lambda_{100} - \lambda_{111})$ value is shown as

$$\lambda_{100} - \lambda_{111} = \frac{16}{3}\left[\overline{\frac{\Delta l}{l}(\psi=0°)} - \overline{\frac{\Delta l}{l}(\psi=45°)}\right]. \tag{27}$$

Figure 10(c) shows the $\overline{\Delta l//l(\psi)}$ measured for the $Fe_{100-x}Co_x(110)$ films. The phase of wave observed for Fe film is in agreement with that of calculated wave of Fig. 10(b-2), whereas the phases of waves measured for $Fe_{70}Co_{30}$ and $Fe_{50}Co_{50}$ films agree with that of wave of Fig. 10(b-1). The result shows that the λ_{100} value is smaller than the λ_{111} value for the Fe film, while the λ_{100} value is larger than the λ_{111} value for the $Fe_{70}Co_{30}$ and the $Fe_{50}Co_{50}$ films. Figure 10(d) shows the $(\lambda_{100} - \lambda_{111})$ values plotted as a function of Co content. As the Co content increases, the $(\lambda_{100} - \lambda_{111})$ value increases. The $Fe_{70}Co_{30}$ and the $Fe_{50}Co_{50}$ films show large $(\lambda_{100} - \lambda_{111})$ values, indicating that large λ_{100} values are obtained.

Large λ_{100} values are obtained, even if Fe-Co films are prepared on MgO substrates with different orientations. Therefore, well-defined epitaxial Fe-Co films have potentials to achieve large magnetostriction.

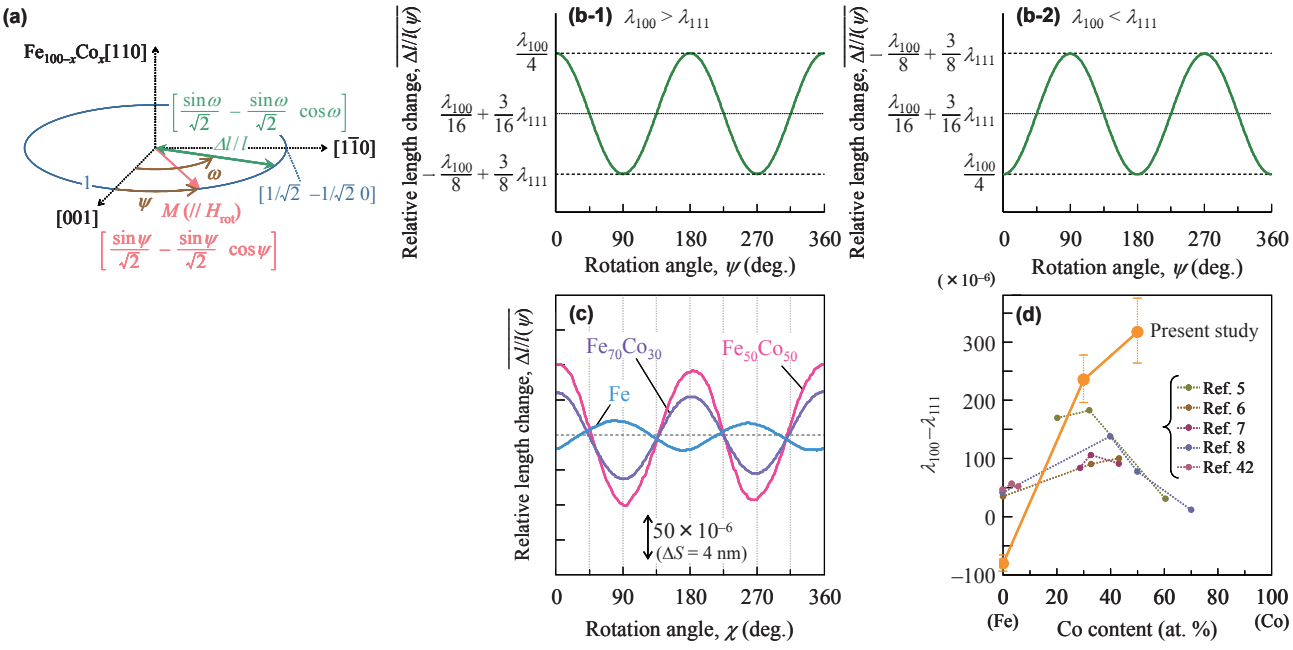

Fig. 10 (a) Schematic diagram showing the magnetization and the observation directions with respect to the typical crystallographic directions. (b) $\overline{\Delta l//l(\psi)}$ calculated for (110) epitaxial multi-crystal films with (b-1) $\lambda_{100} > \lambda_{111}$ and (b-2) $\lambda_{100} < \lambda_{111}$. (c) $\overline{\Delta l//l(\psi)}$ measured for $Fe_{100-x}Co_x(110)$ epitaxial multi-crystal films formed on $MgO(111)/Al_2O_3(0001)$ substrates. (d) Compositional dependences of $(\lambda_{100}-\lambda_{111})$. The bulk values in (d) are calculated by using λ_{100} and λ_{111} values in Refs. 5–8 and 42.

4. Conclusion

$Fe_{100-x}Co_x$ (x = 0–50 at. %) alloy epitaxial films are prepared on MgO substrates with different orientations. The magnetization and the magnetostriction properties are characterized. $Fe_{100-x}Co_x$(001) single-crystal and (211) bi-crystal films are respectively obtained on MgO(001) and (110) substrates, whereas $Fe_{100-x}Co_x$(110) films with nine variants are epitaxially grown on MgO(111) substrates. The (001) single-crystal and the (211) bi-crystal films, respectively, show four- and two-fold symmetric in-plane magnetic anisotropies, which are reflecting the magnetocrystalline anisotropy of $Fe_{100-x}Co_x$ crystal with the easy magnetization axes parallel to <100> or <111>. The easy magnetization directions vary depending on the film composition and orientation. On the contrary, isotropic in-plane magnetization properties are observed for the (110) epitaxial films due to an influence of the variant structure. The magnetostriction behavior under rotating magnetic field is studied. As the Co content increases, the λ_{100} and the λ_{111} values, respectively, increase from $+10^{-5}$ to $+10^{-4}$ and from -10^{-5} to $+10^{-5}$ for both $Fe_{100-x}Co_x$(001) single-crystal and (211) bi-crystal films. Large λ_{100} values are also indicated for the $Fe_{70}Co_{30}$ and the $Fe_{50}Co_{50}$(110) epitaxial films. The present study shows that it is possible to obtain large magnetostriction of 10^{-4} by control of the film orientation and composition.

References

1) A. Ludwig and E. Quandt: *J. Appl. Phys.*, **87**, 4691 (2000).
2) D. Niarchos: *Sens. Actuators A*, **106**, 255 (2003).
3) L. Wang and F. G. Yuan: *Smart Mater. Struct.*, **17**, 045009 (2008).
4) A. E. Clark: *AIP Conf. Proc.*, **34**, 13 (1976).
5) H. M. A. Urquhart, K. Azumi, and J. E. Goldman: *DTIC Tech. Rep.*, no. AD0018771 (1953).
6) R. C. Hall: *J. Appl. Phys.*, **30**, 816 (1959).
7) R. C. Hall: *J. App. Phys.*, **31**, S157 (1960).
8) S. Chikazumi: *Physics of Ferromagnetism* (Syokabo, Tokyo, 1961) pp. 121–122.
9) D. Hunter, W. Osborn, K. Wang, N. Kazantseva, J. Hattrick-Simpers, R. Suchoski, R. Takahashi, M. L. Young, A. Mehta, L. A. Bendersky, S. E. Lofland, M. Wuttig, and I. Takeuchi: *Nat. Commun.*, **2**, 518 (2011).
10) T. Nakajima, T. Takeuchi, I. Yuito, K. Kato, M. Saito, K. Abe, T. Sasaki, T. Sekiguchi, and S. Yamaura: *Mater. Trans.*, **55**, 556 (2014).
11) C. J. Gutierrez, J. J. Krebs, and G. A. Prinz: *Appl. Phys. Lett.*, **61**, 2476 (1992).
12) M. Dumm, M. Zölfl, R. Moosbühler, M. Brockmann, T. Schmidt, and G. Bayreuther: *J. Appl. Phys.*, **87**, 5457 (2000).
13) M. J. Pechan, R. L. Compton, D. Bennett, L. C. Chen, C. J. Palmstrom, and S. J. Allen: *J. Appl. Phys.*, **89**, 7514 (2001).
14) M. Dumm, B. Uhl, M. Zolfl, W. Kipferl, and G. Bayreuther: *J. Appl. Phys.*, **91**, 8763 (2002).
15) S. Park and M. R. Fitzsimmons: *Phys. Rev. B*, **70**, 104406 (2004).
16) Y. Wada, Y. Takahashi, N. Inaba, F. Kirino, M. Ohtake, and M. Futamoto: *J. Magn. Soc. Jpn.*, **37**, 166 (2013).
17) T. Muhge, T. Zeidler, Q. Wang, C. Morawe, N. Metoki, and H. Zabel: *J. Appl. Phys.*, **77**, 1055 (1995).
18) T. H. Kim, Y. H. Jeong, and J. -S. Kang: *J. Appl. Phys.*, **81**, 4764 (1997).
19) H. Tomita, A. Sawabe, T. Sato, and T. Mizoguchi: *Jpn. J. Appl. Phys.*, **34**, 1851 (1995).
20) K. Shikada, M. Ohtake, F. Kirino, and M. Futamoto: *J. Appl. Phys.*, **105**, 07C303 (2009).
21) K. Serizawa, M. Ohtake, M. Futamoto, F. Kirino, and N. Inaba: *J. Magn. Soc. Jpn.*, **41**, 99 (2017).
22) M. Ohtake, K. Serizawa, M. Futamoto, F. Kirino, and N. Inaba: *AIP Adv.*, **8**, 047709 (2018).
23) T. Nishiyama, M. Ohtake, F. Kirino, and M. Futamoto: *J. Appl. Phys.*, **107**, 09A306 (2010).
24) T. Nishiyama, K. Shikada, M. Ohtake, F. Kirino, and M. Futamoto: *J. Magn. Soc. Jpn.*, **34**, 5 (2010).
25) T. A. Lafford, M. R. J. Gibbs, and C. Shearwood: *J. Magn. Magn. Mater.*, **132**, 89 (1994).
26) M. D. Cooke, L. -C. Wang, R. Watts, R. Zuberek, G. Heydon, W. M. Rainforth, and G. A. Gehring: *J. Phys. D: Appl. Phys.*, **33**, 1450 (2000).
27) X. Liu, P. Evans, and G. Zangari: *IEEE Trans. Magn.*, **36**, 3479 (2000).
28) M. D. Cooke, M. R. J. Gibbs, and R. F. Pettifer: *J. Magn. Magn. Mater.*, **237**, 175 (2001).
29) H. S. Jung, W. D. Doyle, J. E. Wittig, J. F. Al-Sharab, and J. Bentley: *Appl. Phys. Lett.*, **81**, 2415 (2002).
30) M. Mao, T. Schneider, R. Bubber, J. Kools, X. Liu, Z. Altounian, C. -L. Lee, A. Devasahayam, and K. Rook: *J. Appl. Phys.*, **97**, 10F908 (2005).
31) Y. Fu, T. Miyao, J. W. Cao, Z. Yang. M. Matsumoto, X. X. Liu, and A. Morisako: *J. Magn. Magn. Mater.*, **308**, 165 (2007).
32) T. Kawai, M. Ohtake, M. Futamoto: *Thin Solid Films*, **519**, 8429 (2011).
33) T. Kawai, T. Aida, M. Ohtake, and M. Futamoto: *J. Magn. Soc. Jpn.*, **39**, 181 (2015).
34) T. Kawai, T. Aida, M. Ohtake, and M. Futamoto: *IEEE Trans. Magn.*, **51**, 2007004 (2015).
35) C. Kittel: *Introduction to Solid State Physics*, 8th ed. (Wiley, Hoboken, 2005) pp. 73–85.
36) K. S. Aleksandrov and T. V. Ryzhova: *Sov. Phys. Crystallogr.*, **6**, 228 (1961).
37) E. R. Dobrovinskaya, L. A. Lytvynov, and V. Pishchik: *Sapphire: Material, Manufacturing, Applications* (Springer, New York, 2009) pp. 95–99.
38) G. Wasserman: *Arch. Eisenhuettenwes*, **16**, 647 (1933).
39) Z. Nishiyama: *Sci. Rep. Tohoku Univ.*, **23**, 638 (1934).
40) G. Kurdjumov and G. Sachs: *Z. Phys.*, **64**, 325 (1930).
41) W. B. Pearson: *A Handbook of Lattice Spacings and Structures of Metals and Alloys* (Pergamon Press, London, New York, Los Angeles, Paris, 1958) pp. 504–505.
42) N. J. Jones, G. Petculescu, M. Wun-Fogle, J. B. Restorff, A. E. Clark, K. B. Hathaway, D. Schlagel, and T. A. Lograsso: *J. Appl. Phys.*, **117**, 17A913 (2015).

Received Nov. 4, 2018; Revised Feb. 15, 2019; Accepted Feb. 27, 2019

J. Magn. Soc. Jpn., **43**, 59-63 (2019)

<Paper>

Suppression of Jahn–Teller distortion by chemical pressure of SiO_2 and local structure analysis of $CuFe_2O_4$ nanoparticles

K. Fujiwara*, S. Kimura*, S. Miyano*, T. Ide*, and Y. Ichiyanagi*,**

*Department of Physics, Graduate School of Engineering, Yokohama National University, 79-5, Tokiwadai, Hodogaya, Yokohama, Kanagawa, 240-8501, Japan

**RCST, Graduate School of Science, Osaka University, 1-1, Machikaneyamacho, Toyonaka, Osaka, 560-0043, Japan

$CuFe_2O_4$ nanoparticles encapsulated by different amounts of amorphous SiO_2 were prepared by a wet chemical method. These nanoparticles were characterized by X-ray diffraction and X-ray absorption fine structure analysis and found to have either a tetragonal or a cubic structure depending on the amount of SiO_2. Magnetization measurements were performed for all samples using a SQUID magnetometer. The tetragonal nanoparticles showed a smaller maximum magnetization (M_S) and a larger coercive force (H_C) than the cubic nanoparticles.

Keywords: Extended X-ray absorption fine structure (EXAFS), Magnetic measurements, Iron oxide, Nano-particles, Magnetization, Nanostructures

1. Introduction

Magnetic nanoparticles have long been of scientific and technological interest. Spinel-structured ferrite nanoparticles with the formula MFe_2O_4 where M represents a divalent metal ion are the most famous magnetic materials and have been used in many industrial applications. The magnetic properties of ferrite nanoparticles were drastically changed by varying the M^{2+} ions and their particle size, which suggests that there are many possibilities for their application by the optimization of their magnetic properties[1)–4)]. In recent years, ferrite nanoparticles have also been investigated for biomedical applications such as magnetic resonance imaging (MRI) enhancement, drug delivery, and heating agents for magnetic hyperthermia[5)–11)].

Copper ferrite ($CuFe_2O_4$) occurs in two structures: tetragonal and cubic. In general, the tetragonal structure is more stable at room temperature and transforms to the cubic structure when heated above about 633–713 K [12) - 15)]. In $CuFe_2O_4$ bulk materials, most of the Cu^{2+} ions occupy the octahedral B sites, meaning that the cation distribution is inverse. Due to this distribution, the orbital overlap between Cu^{2+} and O^{2-} is induced and the octahedral B site distorts from the cubic structure to tetragonal symmetry[16), 17)], which is known as the Jahn–Teller effect. Jahn–Teller distortion only occurs at the B-site; therefore, the distribution of Cu ions affects the structure. The magnetization of $CuFe_2O_4$ is affected by this distortion; the cubic structure has a higher magnetization than the tetragonal structure[18)].

Although $CuFe_2O_4$ nanoparticles can be synthesized by combustion[19)], sol-gel[20),21)], co-precipitation[22)–24)], mechanical milling[25)], and solid-state reactions[26)], there are only a few methods for obtaining size-controlled cubic Cu-ferrite because its structure is greatly affected by the production conditions. For example, the lattice structure is affected by various factors such as lattice defects and heating and cooling speeds. These phenomena are probably caused by the small energy difference between the Cu^{2+} ions that are present at the A-site and B-site[27)]. In our previous studies, we have shown that Cu-ferrite nanoparticles could be obtained by a wet chemical method and that particle diameter can be controlled[28)]. Furthermore, it was possible to encapsulate nanoparticles with amorphous SiO_2 and the structure of Cu-ferrite was affected by the state of the SiO_2. In the present work, we conducted a detailed study of the $CuFe_2O_4$ nanoparticles encapsulated by varying amounts of SiO_2. The $CuFe_2O_4$ nanoparticles were synthesized by the wet chemical method and their fine structure was studied by X-ray diffraction (XRD), X-ray fluorescence (XRF) and X-ray absorption fine structure (XAFS). The magnetic properties of the nanoparticles were also evaluated.

2. Experimental

$CuFe_2O_4$ nanoparticles surrounded by different amounts of amorphous SiO_2 were synthesized by a wet chemical method. Aqueous solutions of $CuCl_2 \cdot 2H_2O$, $FeCl_3 \cdot 6H_2O$, $Na_2SiO_3 \cdot 9H_2O$, and NaOH were mixed to obtain a precipitate by neutralization. The mole ratio of the prepared reagent was Cu:Fe:Si = 1:2:n (n = 0, 0.5, 2, 3, 4) and the amount of SiO_2 was varied according to the mole ratio of $Na_2SiO_3 \cdot 9H_2O$ and NaOH concentration. The obtained precipitates were washed three times with distilled water and dried at about 350 K. The as-prepared samples were then subjected to heat treatment in a furnace under air and at annealing temperatures of ~1023 K, forming $CuFe_2O_4$ in $n$$SiO_2$ (n = 0, 0.5, 2, 3, 4) nanoparticles.

All of the prepared samples were examined by XRD (Cu-Kα, λ = 0.154 nm). The average particle sizes of these samples were estimated by the Scherrer formula and crystallite size distribution analysis software CSDA (RIGAKU). The lattice constants were also calculated by Rietveld analysis using RIETAN-FP software[29)]. In addition, we performed XRF analysis to examine their composition ratios.

X-ray absorption fine structure (XAFS) measurements were performed to clarify the structures of the nanoparticles. The Cu–K edge (8980.3 eV) and Fe–K edge (7,111.2 eV) XAFS spectra were measured in the range of the X-ray absorption near-edge structure (XANES) and the extended X-ray absorption fine structure (EXAFS) spectra were obtained using the transmission method with a Si(111) monochromator at the BL-9C and BL-12C station in the Photon Factory synchrotron radiation facility, KEK, Japan. The cation distribution and atomic distances of samples were analyzed using the fitting software REX2000.

Magnetization measurements were performed using a SQUID magnetometer (Quantum Design, MPMS). Magnetization curves were measured at 5 K in the ±50 kOe applied magnetic field.

3. Results and Discussion

3.1 XRD analysis

Figure 1 shows the XRD patterns of $CuFe_2O_4$ in $n$$SiO_2$ (n = 0, 0.5, 2, 3, 4) nanoparticles annealed at 1023 K. All samples showed a broad peak around 2θ = 23° that corresponded to

amorphous SiO_2. It was evident that these patterns were affected by the amount of SiO_2. The average particle diameters were estimated from the broadening of the diffraction peaks using Scherrer's formula and CSDA and the estimated diameters of all samples were controlled at around 12 nm. The particle diameters were also confirmed by the TEM image (Figure 2). The samples that were rich in SiO_2 (n = 2, 3, 4) showed a single cubic spinel phase (Fd3m). However, the samples without silica (n = 0) and insufficient SiO_2 (n = 0.5) showed multiphase patterns that indicated both cubic and tetragonal spinel phases. Table 1 shows the lattice constants calculated by Rietveld analysis. The axis ratio of the n = 0 sample that showed tetragonal phase was c / a = 1.48.

By the SiO_2 encapsulation, the lattice constants a and b were increased and the lattice structure became cubic. It was considered that the distortion that was caused by different lengths between Cu-O was suppressed by SiO_2 coating. For the cubic samples n = 2, 3, 4, the lattice constants showed almost the same value, so the cubic lattice structure was unchanged by the SiO_2 amount. XRF measurements confirmed that the composition ratio of Cu:Fe maintained the preparation ratio. For the SiO_2, while the ratios were decreased from the preparation ratio, the ratio was changed by n. These XRD patterns led to the conclusion that the crystal structures were affected by the amount of SiO_2 and the $CuFe_2O_4$ nanoparticle's structure became cubic after encapsulation with sufficient SiO_2, $n \geqq 2$. Owing to encapsulation by amorphous SiO_2, $CuFe_2O_4$ was produced with a cubic spinel phase. It is plausible that the amorphous SiO_2 layer suppresses the Jahn–Teller distortion because of pressure from the encapsulated SiO_2. When decreasing the amount of amorphous SiO_2 by using a smaller mole ratio n, the pressure was weakened, which promoted distortion and formed the tetragonal phase.

3.2 XAFS analysis

To investigate the Jahn–Teller distortion and the effect of encapsulation by amorphous SiO_2 on Cu-ferrite nanoparticles, we performed XAFS measurements and analyzed their fine structures. Using XAFS analysis, structural changes such as cation distributions and atomic distances were observed[30].

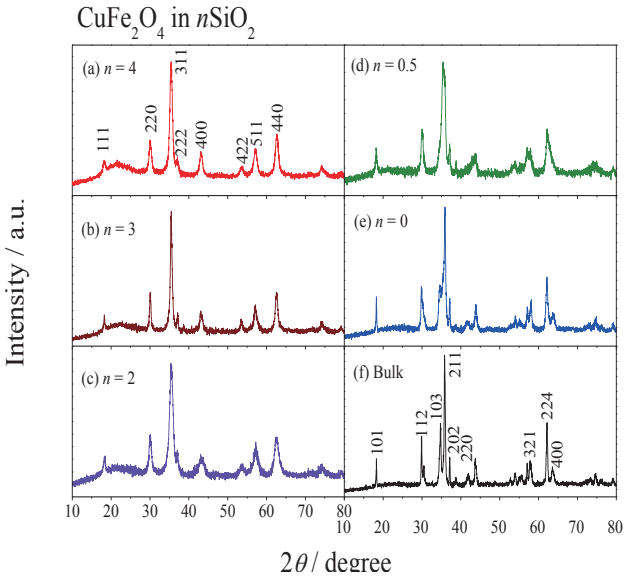

Figure 1. XRD patterns of $CuFe_2O_4$ in $n$$SiO_2$ (n = 0, 0.5, 2, 3, 4) nanoparticles annealed at 1023 K. (a) n = 4, (b) n = 3, (c) n = 2, (d) n = 0.5 and (e) n = 0. (f) XRD pattern of the bulk crystals of $CuFe_2O_4$.

Table 1. The particle diameter and lattice constant values as calculated using the XRD patterns.

SiO_2 amount, n	a / Å	b / Å	c / Å	c / a	Lattice structure
4	8.36	8.36	8.36	1	Cubic
3	8.35	8.35	8.35	1	Cubic
2	8.35	8.35	8.35	1	Cubic
0.5	—	—	—	-	Cubic and Tetragonal
0	5.84	5.84	8.64	1.48	Tetragonal

Table 2. The composition ratios of $CuFe_2O_4$ in $n$$SiO_2$ (n = 0, 0.5, 2, 3, 4) nanoparticles measured by XRF. The ratios were normalized to become $Cu_\alpha Fe_\beta O_4$ in γSiO_2.

SiO_2 amount n	Cu amount α	Fe amount β	Si amount γ
4	1.03	1.97	1.65
3	1.07	1.93	1.54
2	0.96	2.04	0.98
0.5	1.00	2.00	0.31
0	0.98	2.02	0.00

Figure 3 shows the results of the Fourier transformation of the k^3-weighted Cu–K edge and Fe–K edge EXAFS spectra.

In Figure 3(a–d), the first peak at ~1.5 Å corresponds to the distance between the metal ion and its nearest neighbor oxygen atom (M–O). The second peak at ~2.6 Å represents the distance between the two cations in the octahedral B sites (B–B). The third peak at ~3.1 Å represents the distance between a cation in an octahedral B site and a cation in a tetrahedral A site (B–A). Figures 3(a) and (b) illustrate the Cu–K edge spectra of $CuFe_2O_4$ in $n$$SiO_2$ (n = 0, 0.5, 4) nanoparticles; their particle diameter was controlled at around 12 nm. The XRD pattern of the n = 0 sample showed that it possessed a tetragonal spinel structure. Therefore, it was expected that the Cu–O peaks at ~1.5 Å would split into two peaks in the EXAFS spectra. However, the Cu–O

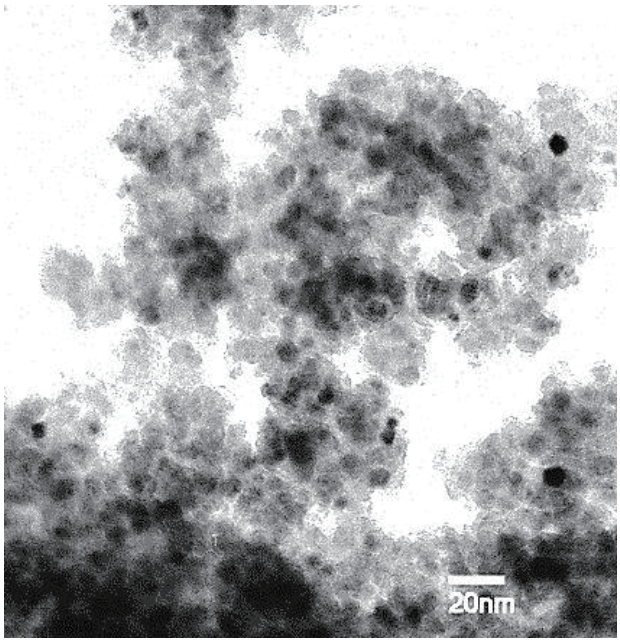

Figure 2. TEM image of 12-nm $CuFe_2O_4$ in $4SiO_2$ nanoparticles.

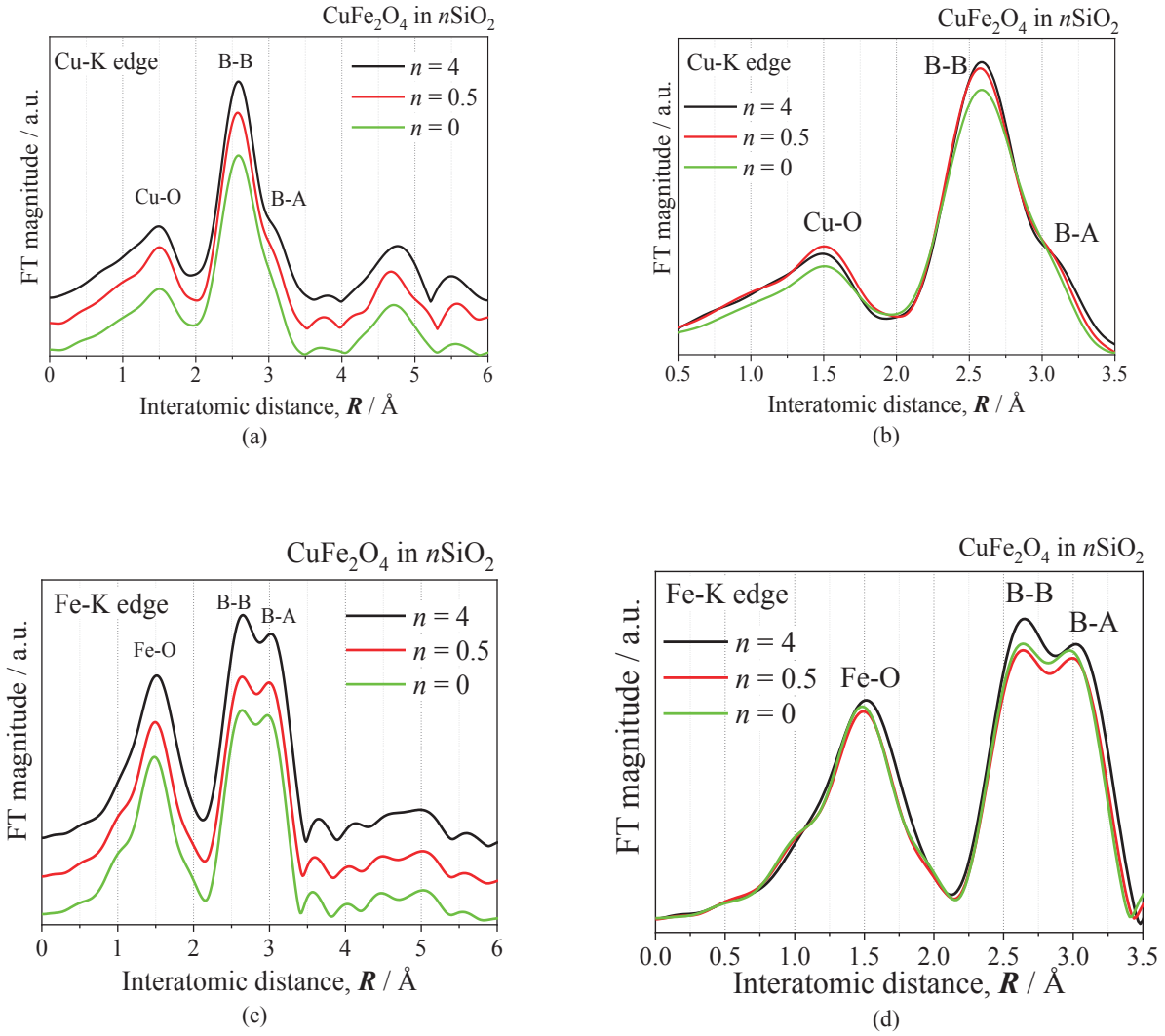

Figure 3. (a) Cu–K edge EXAFS spectra of $CuFe_2O_4$ in $nSiO_2$ (n = 0, 0.5, 4) nanoparticles that were annealed at ~1023 K with particle diameter controlled at approximately 12 nm. (b) Overlapped spectra image of graph (a). (c) Fe–K edge spectra of the nanoparticles in (a). (d) Overlapped spectra image of graph (c).

peaks were single for all samples and the peak intensity weakened as the amount of SiO_2 decreased. The EXAFS spectra consisted of the superposition of sine waves with wavelengths that correspond to the respective atomic distance where similar wavelengths cancel each other out. The weak intensity Cu–O peaks may be explained by the Jahn–Teller distortion effect in this sample's CuO_6 octahedron. Figure 3(a) only showed the B–B peak at ~2.6 Å and no peaks corresponded to the B–A bond at 3.1 Å in the n = 0 and 0.5 samples. However, for the n = 4 sample, there were small shoulders at 3.1 Å that corresponded to the B–A bond. This result suggested that Cu^{2+} ions only became distributed in the tetrahedral A site when n = 4, and this was a typical feature of the cubic structure of Cu-ferrite nanoparticles.

Figures 3(c) and (d) show the Fe–K edge spectra of the $CuFe_2O_4$ in $nSiO_2$ (n = 0, 0.5, 4) samples. The B–B and B–A peaks indicate that the Fe ions occupy both the tetrahedral A sites and the octahedral B sites. Each sample exhibited nearly equal intensities for the B–B and B–A peaks with the n = 0 and 0.5 samples. Therefore, the ratio of Fe ions in the tetrahedral A sites and octahedral B sites would be 1:1. However, the n = 4 sample showed a higher B-B peak than B-A peak, which indicated that the quantity of iron ions distributed in B-site was increased. This result showed good agreement with the result of the Cu-K edge EXAFS spectra. Increasing the amount of Cu^{2+} ions in the A-site squeezed Fe ions into the B-site. This indicated that the ion distribution was closely related to the lattice structure. The distribution change in the metal ions produced the cubic structure of Cu ferrite.

Based on these results, we assumed that the Cu ions occupied

Table 3. M-O length of $CuFe_2O_4$ in $nSiO_2$ (n = 0, 0.5, 4) nanoparticles obtained by EXAFS spectra.

SiO_2 amount, n	Cu-O length / Å	Fe-O length / Å	Lattice structure
4	1.49	1.50	Cubic
0.5	1.50	1.49	Cubic & Tetragonal
0	1.50	1.49	Tetragonal

the remaining octahedral B sites. Therefore, it was reasonable to expect an inverse spinel structure in both samples. In the Fe–K edge spectra, the atomic distance between the iron atoms in the samples with tetragonal structures (n = 0, 0.5) were almost the same as that of the cubic samples. However, more Fe ions were dispersed into the B site in the cubic samples. For the cubic samples, the peak that corresponded to the Cu–O length became stronger and there was a little B–A shoulder in the Cu-K edge spectra. Table 3 shows the M-O length values for each metal ion but does not directly indicate the distortion. We could consider the particle diameter too small to detect the two Cu-O lengths for the tetragonal structure. The peak intensities of Cu-O were changed by n, which we think implied the lattice distortion. Fe ions were more dispersed into the B site in the cubic samples. Considering these experimental results, the distribution change of the metal ions suppressed the Jahn–Teller distortion because that distortion by the Cu^{2+} ions only occurred in the octahedral B-site. This can be explained based on the phenomenon that the amorphous SiO_2 layer decreased the O^{2-} content of the Cu-ferrite nanoparticles, which created defects in the cation structure. Therefore, the energy difference between the Cu^{2+} ions present at the A- and B-sites decreased, so the Cu^{2+} ions could easily occupy the A site and the lattice became cubic[27]. From these results, we concluded that the tetragonal structure was a result of Jahn–Teller distortion in the CuO_6 octahedral coordination and encapsulation by sufficient amorphous SiO_2 suppressed this distortion by causing lattice defects.

3.3 Magnetization measurements

Figure 4 shows the magnetization curves (M–H) of the $CuFe_2O_4$ in $n$$SiO_2$ (n = 0, 0.5, 2, 4) nanoparticles for which their particle diameter was controlled to be approximately 12 nm. The magnetization values of all samples were measured at 5 K in a ±50 kOe field. The magnetization values per unit M were calculated by using the formula:

$$M = \frac{W}{N_A} * m$$

where m is the measured magnetization data divided by the used sample weight, W represents the molecular weight of $CuFe_2O_4$ including SiO_2, and N_A is Avogadro's constant. W was calculated from the composition ratio obtained by XRF analysis. The magnetization value M were expressed by μ_B unit. The saturation magnetization (M_s) of the nanoparticles depends on various amounts of SiO_2: with n = 0, 0.5, 2, and 4, M_S is 1.40, 1.50, 1.78 and 1.94 μ_B, respectively. These results show that the tetragonal spinel samples (n = 0, 0.5) have lower saturation magnetization values than the cubic samples (n = 2, 4). Here, it was expected that the A–B distance (Fe–Cu distance) of the samples that contain less SiO_2 would become shorter than that of the cubic samples because of Jahn–Teller distortion. Thus, different values for the saturation magnetization in Fig. 4 suggest that the interactions between the antiferro-coupling sites A and B change with the A–B distance. This variation in the A–B distance depends on the Cu–O distance caused by Jahn–Teller distortion. The M_S values differed between the cubic samples with n = 2 and 4. The distribution ratios were calculated using their magnetization values and composition ratio: the obtained results were $(Cu_{0.078}Fe_{0.922})[Cu_{0.882}Fe_{1.118}]O_4$ for the n = 2 sample and $(Cu_{0.133}Fe_{0.867})[Cu_{0.897}Fe_{1.103}]O_4$ for the n = 4 sample. From the above, we could confirm that the samples with sufficient silica ($n \geq 2$) gained a cubic structure and that the Cu^{2+} distribution was changed by their structure. For the cubic samples n = 2 and 4, the lattice constant and their composition ratio of metal ions were almost the same. The difference in the samples was only in the amount of SiO_2. These results showed that the difference in M_S between the cubic samples with n = 2 and 4 was caused by their different distributions of metal ions. This implied that the Cu^{2+} ions distribution was changed by the SiO_2 amount for the cubic samples.

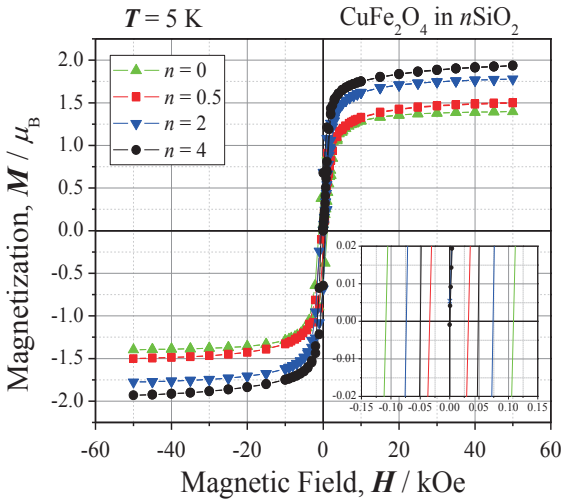

Figure 4. Magnetization curves at 5 K of $CuFe_2O_4$ in $n$$SiO_2$ (n = 0, 0.5, 2, 4) nanoparticles with diameter controlled to around 12 nm.

4. Conclusions

The SiO_2 encapsulation effects were investigated for the $CuFe_2O_4$ nanoparticles. The Cu ferrite encapsulated by different amounts of amorphous SiO_2 was synthesized using a wet chemical method. XRD patterns showed that the structure of the nanoparticles was changed by the amount of added SiO_2 and their particle diameters were controlled around 12 nm. EXAFS analysis clarified that the encapsulation by amorphous SiO_2 distributed Cu ions into the tetrahedral A-site and the structure became cubic upon sufficient silica encapsulation. Magnetization measurements showed that the cubic-structure sample had a higher M_S value than that of the sample with the tetragonal structure. This result was caused by the change in the lattice structure and the difference in Cu^{2+} ions distribution.

Acknowledgments

This study was partially supported by Precursory Research for Embryonic Science and Technology at the Japan Science and Technology Agency, JST-Mirai Program No. JPMJMI17D7, and a Grant-in-Aid for Science Research (No. 25286041) from the Japan Society for the Promotion of Science (JSPS).

References

1) C. Liu and Z. J. Zhang: *Chem. Mater.*, **13**, 2092 (2001)
2) A. Manikandan, L. J. Kennedy, M. Bououdina and J. J. Vijaya: *J. Magn. Magn. Mater.*, **349**, 249 (2014)
3) M. K. Roy and H.C. Verma: *J. Magn. Magn. Mater.*, **306**, 98 (2006)
4) A. Kale, S. Gubbala and R. D. K. Misra: : *J. Magn. Magn. Mater.*, **277**, 350 (2004)
5) B. Chertok, B. A. Moffat, A. E. David, F. Yu, C. Bergemann, B. D. Ross and V. C. Yanga: *Biomaterials*, **29**, 487 (2008)
6) A. H. Rezayan, M. Mousavi, S. Kheirjou, G. Amoabediny, M. S. Ardestani and J. Mohammadneja: *J. Magn. Magn. Mater.*, **420**, 210 (2016)

7) A. Jordan, R. Scholz, P. Wust, H. Fähling and R. Felix: *J. Magn. Magn. Mater.,* **201**, 413 (1999)
8) D. H. Kim, D. E. Nikles, D. T. Johnson and C. S. Brazel, *J. Magn. Magn. Mater.,* **320**, 2390 (2008)
9) J. Lu, S. Ma, J. Sun, C. C. Xia, C. Liu, Z. Wang, X. Zhao, F. Gao, Q. Gong, B. Song, X. Shuai, H. Ai and Z. Gu, *Biomaterials*, **30**, 2919 (2009)
10) M. Suto, Y. Hirota, H. Mamiya, A. Fujita, R. Kasuya, K. Tohji and B. Jeyadevan: *J. Magn. Magn. Mater.,* **321**, 1493 (2009)
11) T. Kondo, K. Mori, T. Yamazaki, D. Okamoto, M. Watanabe, K. Gonda, H. Tada, Y. Hamada, M. Takano, N. Ohuchi and Y. Ichiyagnagi: *Jour. Appl. Phys.*, **117**, 17D157 (2015)
12) H. Ohnishi and T. Teranishi, *J. Phys. Soc. Jpn.*, **16** (1), 35 (1961)
13) J. Darul: *Z. Kristallogr. Suppl.*, **30**, 335 (2009)
14) A. M. Balagurov, I. A. Bobrikov, M. S. Maschenko, D. Sangaa and V. G. Simkin: *Crystallogr. Rep.*, **58**, 710 (2013)
15) A. M. Balagrov, I. A. Bobrikov, V. Y. Pomjakushin, D. V. Sheptyakov and V. Y. Yushankhai: *J. Magn. Magn. Mater.,* **374**, 591 (2015)
16) H. A. Jahn and E. Teller: *Proc. R. Soc. Lond. Ser. A Math. Phys. Sci.*, **161** (905), 220 (1937)
17) J. B. Goodenough and A. L. Loeb: *Phys. Rev.*, **98** (2), 391 (1955)
18) M. A. Amer, T. Meaz, A. Hashhash, S. Attalah and F. Fakhry: *J. Alloy. Com.*, **649**, 712 (2015)
19) V. Krishnan, R. K. Salvan, C. O. Ausustin, A. Gedanken and H. Bertanolli: *J. Phys. Chem. C*, **111**, 16724 (2007)
20) P. Laokul, V. Amornkitbamrung, S. Seraphin and S. Maensiri, *Curr. Appl. Phys.*, **11**, 101 (2011)
21) F. Caddeo, D. Loche, M. F. Casula and A. Corrias, *Sci. Rep.*, **8**, 797 (2018)
22) S. Sultana, Rafiuddin, M. Z. Khan and K. Umar, *J. Alloy. Com.*, **535**, 44 (2012)
23) M. Kanagaraj, P. Sathishkumar, G. K. Selvan, I. P. Kokila and S. Arumugam: *Indian J. Pure and Appl. Phys.*, **52**, 124 (2014)
24) E. Agouriane, B. Rabi, A. Essoumhi, A. Razouk, M. Sahlaoui, B. F. O. Costa and M. Sajieddine: *J. Mater. Environ. Sci.*, **7**, 4116 (2016)
25) G. F. Goya and H. R. Rechenberg: *J. Appl. Phys.*, **84** (2), 1101 (1998)
26) Z. Sun, L. Liu, D. Z. jia and W. Pan: *Sens. Actuators B*, **125**, 144 (2007)
27) Y. Uehara: *Zairyou,* **22**, pp. 96 (1973)
28) S. Kimura, T. Mashino, T. Hiroki, D. Shigeoka, N. Sakai, L. Zhu and Y. Ichiyanagi: *Thermochemica Acta*, **532**, 119 (2012)
29) F. Izumi and K. Momma, *Solid State Phenom*., **130**, 15 (2007)
30) I. Nakai, K. Takahashi, Y. Shiraishi, T. Nakagome and F. Nishikawa: *J. Solid. State. Chem.*, **140**, 145 (1998)

Received Oct. 26, 2018; Revised Dec. 24, 2018; Accepted Mar. 2, 2019

J. Magn. Soc. Jpn., **43**, 64-69 (2019)

<Paper>

Integrated CMOS Switch Buck DC-DC Converter Fabricated in Organic Interposer with Embedded Magnetic Core Inductor

T. Akiyama, S. Ishida, T. Shirasawa, T. Fukuoka, S. Hara, H. Yoshida, M. Sonehara, T. Sato, and K. Miyaji

Spin Device Technology Center, Shinshu Univ., *4-17-1 Wakasato, Nagano 380-8553, Japan*

In this paper, the development of a CMOS switch buck DC-DC converter fabricated in an organic interposer with an embedded power inductor is described. The power inductor is fabricated by using a magnetic core made of an Fe-based amorphous alloy powder-filler/epoxy composite sheet to form a fully closed magnetic circuit and is embedded in the organic interposer in a lamination process. The fabricated power inductor is located under a CMOS control chip and has a of 3.5-mm-square footprint. The CMOS switch buck DC-DC converter runs at 20 MHz, and the fabricated power inductor has an inductance of 150 nH and Q-factor of 38 at around 20 MHz. Furthermore, the influence of magnetic flux leakage from the embedded power inductor to a copper wiring pattern on the surface was analyzed in a simulation that utilized three-dimensional electromagnetic field analysis software (ANSYS; HFSS). Based on the simulation result, the conduction losses of the inductor were calculated under the assumption of use in a synchronous buck converter operating with a 5-V input and 3.3-V 0.8-A output.

Keywords: power inductor, organic interposer, Fe-based amorphous alloy powder-filler/epoxy composite sheet, lamination process, DC-DC converter

1. Introduction

In recent years, power distribution losses between power supply and the loads have increased due to requirement of low-voltage and high-current loads such as LSIs. In order to reduce the power distribution loss, the distributed power architecture with Point of Load (POL) DC-DC converters has been widely used[1),2)]. However, development of the small power inductor is desired because the POL DC-DC converter occupy considerable footprint on the mother board[3),4)]. The package integrated power inductor has been studied[5),6)] to make POL converter footprint smaller. INTEL has developed package-integrated POL converter using air-core solenoid inductor for their fourth-generation core processor Haswell[7)]. The air-core inductor can be easily fabricated by only the metal process, but has serious disadvantages such as low inductance value and undesired EMI noise due to widespread alternating magnetic flux[8)]. In order to reduce the footprint and reduce the EMI noise, it is expected to introduce a magnetic core in the inductor.

This paper describes the development of power inductor using soft magnetic powder-filler/epoxy composite sheets as a magnetic core. The embedded power inductor in the organic interposer is made by lamination process. Furthermore, CMOS control flip-chip IC and other Surface Mount Devices (SMD) are mounted on the organic interposer by reflow soldering at 180°C to fabricate 20 MHz switching buck DC-DC converter. The simulation results focusing on the influence of leakage magnetic from the power inductor to the surface wiring copper pattern at 20 MHz are also described. Surface wiring copper pattern locates just above the embedded power inductor and form a surface layer of the organic interposer which CMOS control chip and SMDs are mounted.

2. Outline of organic interposer

Figure 1 shows a cross-section view of the power inductor embedded in the organic interposer with 1.6 mm thick glass-fiber/epoxy center core and 50 μm thick glass-filler/epoxy build-up layer. The glass-filler/epoxy build-up layer is formed by thermal laminator in the organic interposer fabrication process. In this work, the magnetic core power inductor embedded in the organic interposer is based on the conventional lamination process using soft magnetic powder-filler/epoxy build-up sheet. The soft magnetic powder-filler/epoxy composite sheet changed the glass-filler to soft magnetic powder-filler. In this method, it is unnecessary to change the conventional organic interposer fabrication process but only changing the laminating condition of the composite sheet[9)].

3. Fe-based amorphous alloy powder-filler/epoxy composite sheet

The magnetic composite sheet consist of 2.56 μm-median diameter Fe-based amorphous alloy powder ($Fe_{87.83}Si_{6.59}B_{2.54}Cr_{2.53}C_{0.51}$ (wt.%)) and epoxy resin.

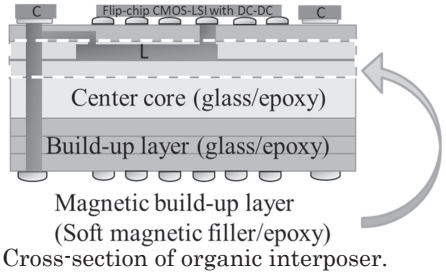

Fig. 1 Cross-section of organic interposer.

Figure 2 shows the static magnetization curve and complex permeability of amorphous alloy powder-filler/epoxy composite sheet measured using VSM (Vibrating-sample magnetometer, Riken Denshi; BHV-55), and RF Impedance/Material Analyzer (Hewlett-Packard; HP4291B) with coaxial waveguide. The saturation magnetization of Fe-based amorphous alloy powder-filler/epoxy composite sheet is about 0.8 T. A filling ratio of Fe-based amorphous alloy powder-filler in the composite sheet is estimated at 64 vol.%. The relative permeability μ' is about 9 at tens MHz. Also, the imaginary part of the complex permeability μ'' related to magnetic loss is small up to around tens MHz. Furthermore, the coercivity of the amorphous powder-filler/epoxy composite sheet measured using coercivity meter (Denshijiki Industory; HC-1031) is 324 A/m (4 Oe).

4. Fabrication process of the power inductor

In the organic interposer, the Fe-based amorphous alloy powder-filler/epoxy composite sheet layer is formed by thermal lamination process. Since the composite sheet has a characteristic of thermoplastic and becomes soft at high temperature, the composite sheet is pressed and laminated to the FR-4 base substrate while it is heated at 150°C. By heating the composite sheet, it is possible to fill the composite material between the thick film coil conductors having large unevenness shown in Fig. 3 and can maintain the planarization of the composite sheet surface[10]. The base substrate and the composite sheet is heated at 150°C, then 190°C post curing is performed in a clean oven after the lamination.

The power inductor is embedded in the organic interposer according to the fabrication procedure shown in Fig. 4. A copper spiral coil having a thickness of 70 μm is fabricated by electroplating process using photo resist lift-off process. The power inductor embedded in the Fe-based amorphous alloy powder-filler/epoxy composite sheet and forms a fully closed magnetic circuit.

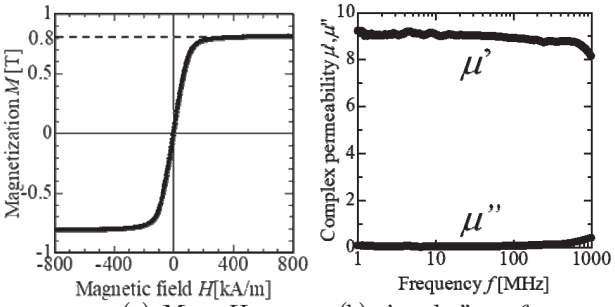

(a) M *vs.* H (b) μ' and μ'' *vs.* f

Fig. 2 (a) Static magnetization curve and (b) complex permeability versus frequency of Fe-based amorphous alloy powder-filler/epoxy composite sheet.

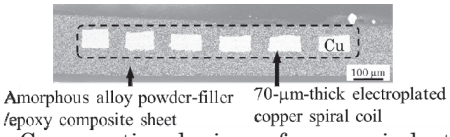

Fig. 3 Cross-sectional view of power inductor with height of about 70 μm and Fe-based amorphous alloy powder-filler/epoxy composite sheet.

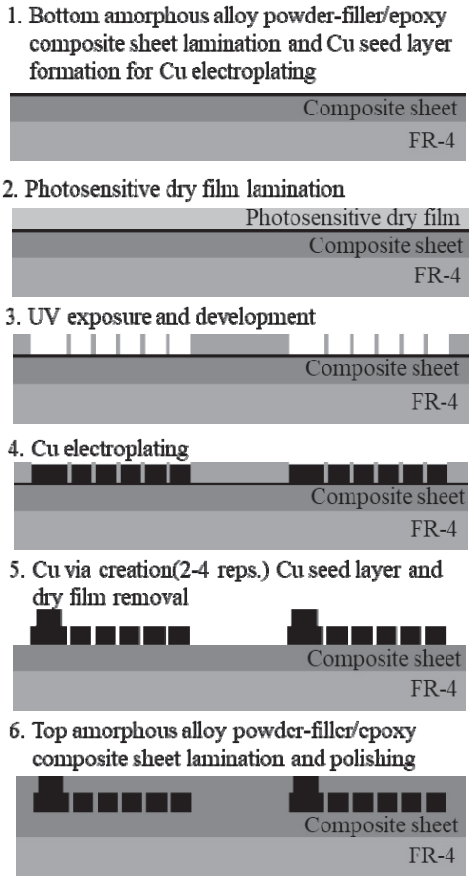

Fig. 4 Process for fabricating power inductor.

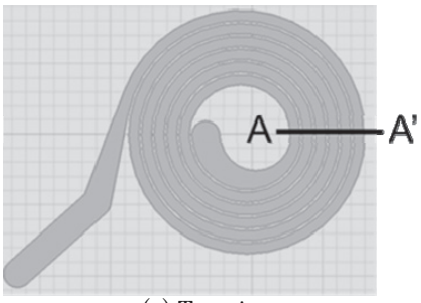

(a) Top view

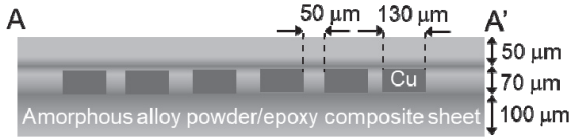

(b) Cross-sectional view

Fig. 5 Structure of power inductor consisting of 6-turn 70-μm-thick copper spiral coil embedded in Fe-based amorphous alloy powder-filler/epoxy composite sheet.

5. Power inductor using Fe-based amorphous alloy powder/epoxy composite sheet

5.1 Power inductor structure

Figure 5 shows the structure of the power inductor. A 70 μm thick electroplated copper 6-turn spiral coil winding with 130/50 μm line/space and 3.5 mm-square foot-print, has a DC coil resistance of 170 mΩ.

5.2 Electrical characteristics of power inductor

Figure 6 shows the measurement result of the electrical characteristics of the fabricated power inductor using RF Impedance/Material Analyzer (Hewlett-Packard; HP4291B) and simulation result of utilizing three-dimensional electromagnetic field analysis software (ANSYS; HFSS). As shown in Fig. 6, the inductance decrease slightly and equivalent series resistance increase with increasing frequency. Since the 6-turn spiral coil has 130 μm wide conductor lines, it is considered that skin effect and proximity effect in the conductor width direction cause the inductance to decrease and equivalent series resistance to increase. The fabricated power inductor has 150 nH at 20 MHz, which was almost the same value as the simulation result. Q-factor of fabricated power inductor was 38 at 20 MHz, which was 24% lower than the simulation result. Since the inductance is almost the same as the simulation result, the cause of the decrease in the Q-factor is an increase in the equivalent series resistance. The main reason for the increase in equivalent series resistance is presumed to be the contact resistance between the spiral coil and the via conductor and the parasitic resistance at the time of measurement. Furthermore, the peak of the Q-factor was about 40 MHz, it is necessary to change the structure of the power inductor and the filling ratio of Fe-based amorphous alloy powder of the composite sheet for that the peak value becomes 20 MHz.

5.3 Organic interposer integrated CMOS switch buck DC-DC converter

The surface wiring copper pattern formed just above the embedded power inductor made by electroplating process which is mount for CMOS control chip and SMD. The appearance of the fabricated the organic interposer integrated CMOS switch buck DC-DC converter is shown in Fig. 7. The footprint including the CMOS control chip and SMD is 7.2 mm x 6.0 mm. The X-ray photograph shows the power inductor is laid out under CMOS control chip and SMD.

5.4 Influence of surface wiring pattern formed above the power inductor

The eddy current is generated on the surface wiring copper pattern due to the leakage magnetic flux from the embedded power inductor. The magnetic flux generated by this eddy current has an opposite direction to the main magnetic flux from the power inductor and decrease of the Q-factor of the power inductor. In this section, the influence of leakage magnetic flux from the embedded power inductor to the surface wiring copper pattern has been analyzed by simulation utilizing three-dimensional electromagnetic field analysis software. A Simulation model is shown in Fig. 8. The analysis condition is a sine wave with an effective value of 1 A flow at 20 MHz.

Figure 9 shows the magnetic flux density distribution of the cross-section A-A' of the power inductor (Fig. 8(b)). From Fig. 9, It can be confirmed from the figure that the leakage magnetic flux is generated from the power inductor to the surface wiring copper pattern.

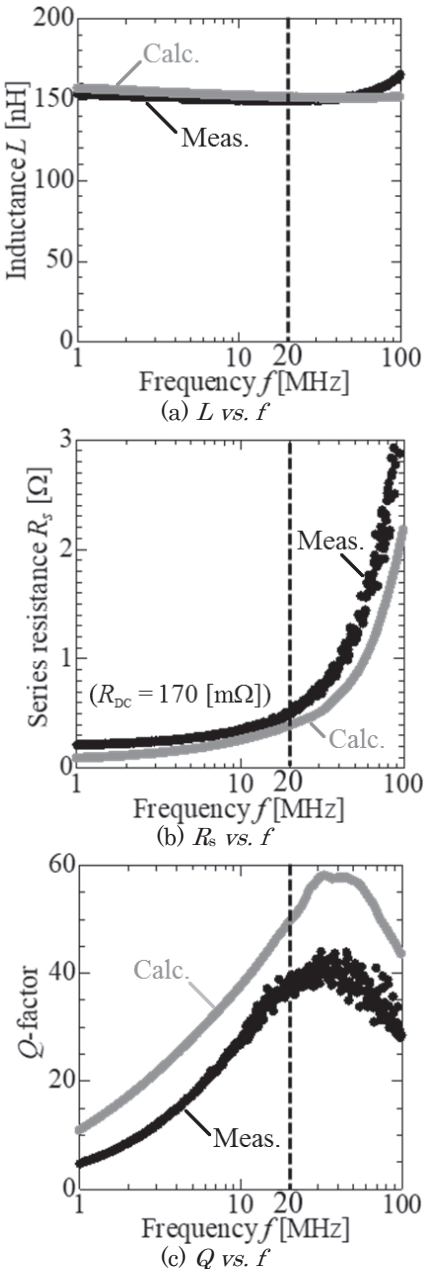

Fig. 6 Measured and simulated (a) inductance L, (b) equivalent series resistance R_s, and (c) Q-factor versus frequency f.

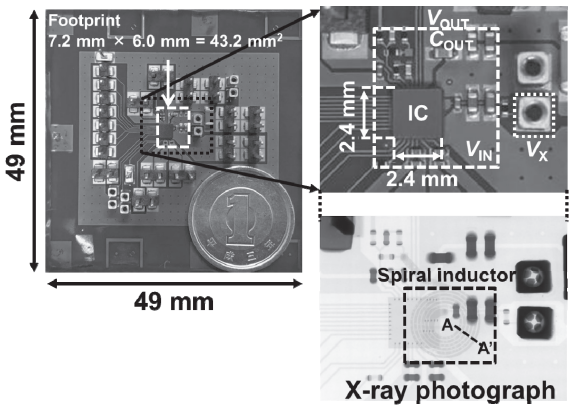

Fig. 7 Photograph of fabricated CMOS switch buck DC-DC converter.

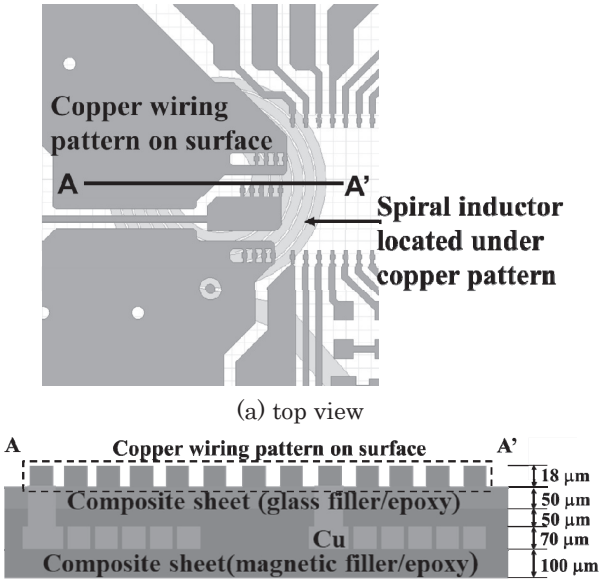

(a) top view

(b) cross view

Fig. 8 Simulation model (a) top view and (b) cross view.

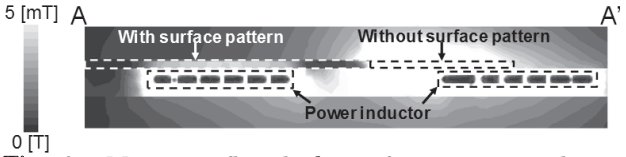

Fig. 9 Magnetic flux leakage from power inductor (cross view, contour).

Figure 10 shows the current density distribution of the surface wiring copper pattern. The eddy current on the surface wiring copper pattern is generated by leakage magnetic flux from the power inductor embedded in the organic interposer. The eddy current flows on the surface wiring copper pattern increase the equivalent series resistance of the power inductor. Furthermore, the magnetic flux generated by the eddy current decrease main magnetic flux from the power inductor and its inductance value. It might be necessary to increase the relative permeability of the composite sheet and to increase the distance between the surface wiring copper pattern and the power inductor in order to the influence of the leakage magnetic flux.

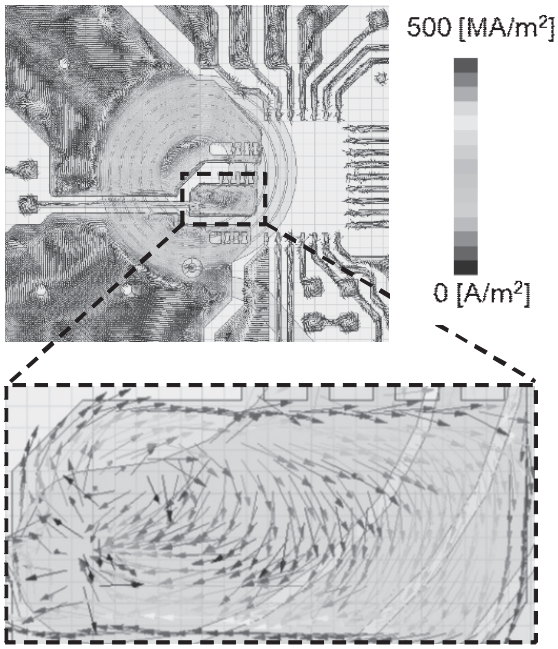

Fig. 10 Eddy current generated on copper wiring pattern on surface (top view, vector).

Figure 11 shows the simulation result of frequency characteristics of inductance L, equivalent series resistance R_s', and Q'-factor with and without the surface wiring copper pattern. At 20 MHz, the inductance decreased by 14%, the Q'-factor decreased by 58% and the equivalent series resistance increases by 88% due to the influence of the surface wiring copper pattern just above the embedded power inductor. The main reason for lowing the Q'-factor is the increase of equivalent series resistance due to the eddy currents in the surface wiring copper pattern caused by leakage flux from the embedded power inductor. In case of the surface wiring copper pattern just above the power inductor, the equivalent series resistance becomes large, so it is necessary to consider the inductor conduction loss.

5.5 Inductor conduction loss

Figure 12 shows an equivalent circuit of the synchronous buck DC-DC converter. Since capacitance C in Fig. 12 is considered to besufficiently large, the inductor current waveform of the DC-DC converter using ideal inductor is a triangular wave as shown in Fig. 13. The inductor current increase/decrease linearly during on/off of the high side switch S_1. When the inductor current is a triangular wave, the amplitude of the ripple current is expressed by Eq. (1).

$$I_R = V_{in} D (1 - D) / 2 f L \qquad (1)$$

The specification of the synchronous buck DC-DC converter are listed in Table 1 and as follows, input voltage; 5 V, load current; 0.8 A and constant on-duty ratio D of high-side switch; 0.66. The effective value of the inductor current is expressed by Eq. (2).

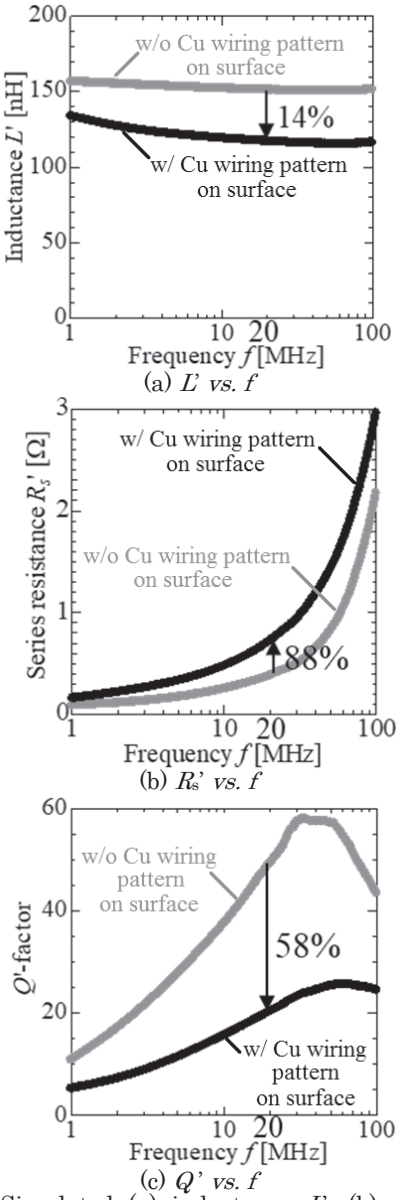

Fig. 11 Simulated (a) inductance L', (b) equivalent series resistance R_s', and (c) Q'-factor versus frequency f with and without copper wiring pattern on surface.

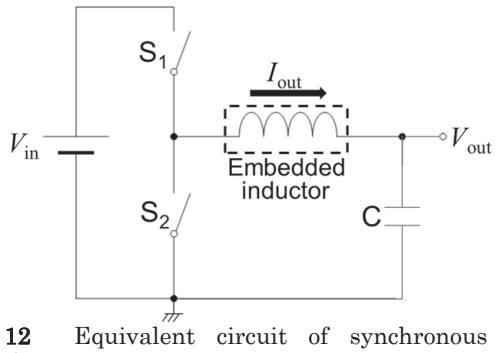

Fig. 12 Equivalent circuit of synchronous buck converter.

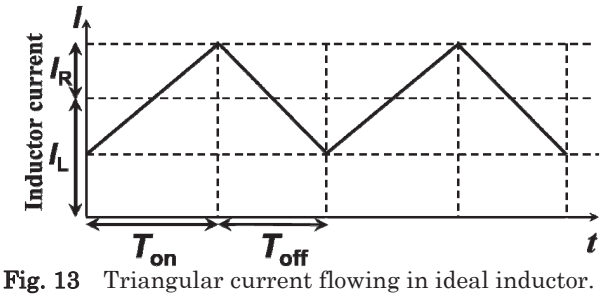

Fig. 13 Triangular current flowing in ideal inductor.

Table 1 Specifications of buck DC-DC converter fabricated in organic interposer.

Item	Specification
Input voltage, V_{in}	5.0 V
Output voltage, V_{out}	3.3 V
Load current, I_L	0.80 A

Table 2 AC conduction loss of power inductor.

Item	AC conduction loss @ 20 MHz
P_{AC} (w/o surface pattern)	3.90 mW
P_{AC} (w/ surface pattern)	12.6 mW

$$I_{rms}^2 = (I_L^2 + I_R^2 / 3) \quad (2)$$

I_L is a direct current superimposed current flowing in the inductor, which is the output current of the DC-DC converter. Therefore, the conduction loss P of the inductor in the operating state of the DC-DC converter can be expressed by Eq. (3).

$$P = R\,(I_L^2 + I_R^2 / 3) = R_{dc}\, I_{out}^2 + R_s\, I_R^2 / 3 \quad (3)$$

The conduction loss of the fabricated inductor is calculated by using Eq. (3), the DC conduction loss is 108.8 mW and the AC conduction loss is 5.8 mW. The AC conduction loss of power inductor with and without surface wiring copper pattern are shown in Table 2. Despite the increase in the AC conduction loss of the power inductor due to the influence of the surface wiring copper pattern, the DC conduction loss is much larger than the AC conduction loss. The large DC resistance of the power inductor results in the decrease of power conversion efficiency for CMOS switch buck DC-DC converter. It is necessary to study the structure of the power inductor and increase the relative permeability of the non-magnetic resin/soft magnetic filler composite sheet to achieve low DC resistance.

6. Conclusions

The CMOS switch buck DC-DC converter fabricated in the organic interposer with an embedded amorphous alloy powder-filler/epoxy composite sheet core inductor made by lamination process was developed and evaluated. The developed amorphous alloy powder-filler/epoxy composite sheet core inductor has a footprint of 3.5 mm square, inductance of 150 nH, Q factor of 38 at around 20 MHz. Although the Q-factor decrease due to the influence of the surface wiring copper pattern just above the embedded power inductor, it did not lead to large increase of the inductor power loss. The most important issue for power loss is the large DC resistance of the power inductor. The large DC resistance of the power inductor decrease power conversion efficiency of CMOS switch buck DC-DC converter.

In the future work, authors will investigate the novel structure and soft magnetic-filler/non-magnetic resin composite sheet design to achieve low DC resistance and high Q-factor power inductor.

Acknowledgments This research was partially supported by Semiconductor Technology Academic Research Center (STARC), and JST-Mirai Program "Realization of a low carbon society through game changing technologies", Japan.

The authors thank Researcher Toshitaka Minamisawa, Shinshu University, for assisting the experiment of power supply circuit.

References

1) H. Kobayashi, F. Sato, K. Hagita, R. Takeda, M. Sonehara, T. Sato, N. Matsushita, K. Kobayashi, H. Shimizu, T. Fujii, K. Ishida, and T. Sakurai: *J. Magn. Soc. Jpn.* (in Japanese), **37**, 4. pp.314-319 (2013).
2) X. Zhou, P. L. Wong, P. Xu, F. C. Lee, and A. Q. Huang: *IEEE Trans. Pwr. Elec.*, **15**, 6, pp.1172-1182 (2000).
3) S. Ji: *Master of Sci Dissertation, Virginia Tech.*, (2013).
4) Y. Su: *Ph.D. Dissertation, Virginia Tech.*, (2014).
5) K. Hagita, Y. Yazaki, Y. Kondo, M. Sonehara, T. Sato, T. Fujii, K. Kobayashi, S. Nakazawa, H. Shimizu, T. Watanabe, Y. Seino, N. Matsushita, Y. Yanagihara, T. Someya, H. Fuketa, M. Takamiya, and T. Sakurai: *J. Magn. Soc. Jpn.*, **39**, 2, pp.71-79 (2015).
6) J. Wibben, and R. Harjani: *IEEE JSSC*, **43**, 4, pp.844-854 (2008).
7) N. Kurd, M. Chowdhury, E. Burton, T. P. Thomas, C. Mozak, B. Boswell, P. Mosalikanti, M. Neidengard, A. Deval, A. Khanna, N. Chowdhury, R. Rajwar, T. M. Wilson, and R. Kumar: *IEEE JSSC*, **50**, 1, pp.49-58 (2015).
8) W. J. Lambert, M. J. Hill, K. Radhakrishnan, L. Wojewoda, and A. E. Augustine: *IEEE Trans. CPMT*, **6**, 1, pp.3-11 (2016).
9) H. Yamaguchi, R. Oka, T. Akiyama, T. Sato, M. Sonehara, and K. Miyaji: *The Annual Meeting Record IEEJ 2017* (in Japanese), 2-118, (2017).
10) T. Akiyama, R. Oka, H. Yamaguchi, T. Sato and M. Sonehara: *The Paper of Technical Meeting on Magnetics and Linear Drives, IEE Japan* (in Japanese), MAG-17-070/LD-17-038, pp.47-52 (2017).

Received Jan. 20, 2019; Revised Mar. 06, 2019; Accepted Mar. 15, 2019

Editorial Committee Members・Paper Committee Members

Notice for Photocopying

編 集 委 員・論 文 委 員

複写をされる方へ

Journal of the Magnetics Society of Japan

Vol. 43 No. 3 (通巻第 303 号) 2019 年 5 月 1 日発行

Vol. 43 No. 3 Published May. 1, 2019
by the Magnetics Society of Japan
Tokyo YWCA building Rm207, 1–8–11 Kanda surugadai, Chiyoda-ku, Tokyo 101–0062
Tel. +81–3–5281–0106 Fax. +81–3–5281–0107

Printed by JP Corporation Co., Ltd.
Sports Plaza building 401, 2–4–3, Shinkamata Ota-ku, Tokyo 144–0054
Advertising agency: Kagaku Gijutsu-sha

発行：(公社)日本磁気学会 101–0062 東京都千代田区神田駿河台 1–8–11 東京YWCA会館 207 号室
製作：ジェイピーシー 144–0054 東京都大田区新蒲田 2–4–3 スポーツプラザビル401 Tel.（03）6715–7915
広告取扱い：科学技術社 111–0052 東京都台東区柳橋 2–10–8 武田ビル 4F Tel.（03）5809–1132